

Motion of a rigid particle in a rotating viscous flow: an integral equation approach

By JOHN P. TANZOSH AND H. A. STONE

Division of Applied Sciences, Harvard University, Cambridge, MA 02138, USA

(Received 29 October 1993 and in revised form 29 March 1994)

A boundary integral method is presented for analysing particle motion in a rotating fluid for flows where the Taylor number \mathcal{T} is arbitrary and the Reynolds number is small. The method determines the surface traction and drag on a particle, and also the velocity field at any location in the fluid.

Numerical results show that the dimensionless drag on a spherical particle translating along the rotation axis of an unbounded fluid is determined by the empirical formula $D/6\pi = 1 + (4/7)\mathcal{T}^{1/2} + (8/9\pi)\mathcal{T}$, which incorporates known results for the low and high Taylor number limits. Streamline portraits show that a critical Taylor number $\mathcal{T}_c \approx 50$ exists at which the character of the flow changes. For $\mathcal{T} < \mathcal{T}_c$ the flow field appears as a perturbation of a Stokes flow with a superimposed swirling motion. For $\mathcal{T} > \mathcal{T}_c$ the flow field develops two detached recirculating regions of trapped fluid located fore and aft of the particle. The recirculating regions grow in size and move farther from the particle with increasing Taylor number. This recirculation functions to deflect fluid away from the translating particle, thereby generating a columnar flow structure. The flow between the recirculating regions and the particle has a plug-like velocity profile, moving slightly slower than the particle and undergoing a uniform swirling motion. The flow in this region is matched to the particle velocity in a thin Ekman layer adjacent to the particle surface.

A further study examines the translation of spheroidal particles. For large Taylor numbers, the drag is determined by the equatorial radius; details of the body shape are less important.

1. Introduction

This paper presents an integral equation solution for analysing particle motion through fluids undergoing solid-body rotation. The approach accounts for Coriolis and centrifugal forces, but neglects the local and convective accelerations as measured in a rotating frame. The mathematical framework extends the boundary integral method for Stokes flows to the class of linearized, rotating viscous flows. To demonstrate the method, we determine the drag and the velocity field generated by an isolated axisymmetric particle translating parallel to the rotation axis in an unbounded fluid.

Particle motion in a rotating fluid may be characterized by the Taylor number \mathcal{T} and Reynolds number \mathcal{R}_e defined as

$$\mathcal{R}_e \equiv \frac{U_p a}{\nu} \quad \text{and} \quad \mathcal{T} \equiv \frac{\Omega a^2}{\nu}, \quad (1.1)$$

\mathcal{T}	Shape	Method	Reference
0	sphere	exact solution	Stokes
$\ll 1^\dagger$	sphere	matched asymptotic expansion	Childress (1964)
$\gg 1$	ellipsoid	unsteady, inviscid analysis	Stewartson (1952)
$\gg 1$	disc/sphere	boundary-layer analysis	Morrison & Morgan (1956)
$\gg 1$	disc/sphere	boundary-layer analysis	Moore & Saffman (1969)
$\gg 1$	bubble/drop	boundary-layer analysis	Bush <i>et al.</i> (1993)
arbitrary	sphere	multipole expansion	Weisenborn (1985)
arbitrary	disc	dual integral equations	Vedensky & Ungarish (1994)
< 1	sphere	numerical: finite difference, series expansion ($\mathcal{R}_e < 1$)	Dennis <i>et al.</i> (1982)

TABLE 1. An overview of theoretical work related to slow particle motion ($\mathcal{R}_e \ll 1$) along the rotation axis of an unbounded fluid in solid-body rotation. (Dennis *et al.* 1982 included weak inertial effects so that $\mathcal{R}_e < 1$.) $^\dagger \mathcal{R}_e/\mathcal{T}^2$ fixed.

where a is a representative particle dimension, U_p is the particle velocity, Ω is the solid-body rotation rate, and ν is the kinematic viscosity. The Taylor number expresses the relative importance of the Coriolis to the viscous forces. Different non-dimensional parameters often appear in the rotating-fluids literature. For example, fluid motion is commonly characterized using the Rossby number $\mathcal{R}_o \equiv U_p/\Omega a = \mathcal{T}^{-1} \mathcal{R}_e$ and Ekman number $E_k = \nu/\Omega a^2 = \mathcal{T}^{-1}$.

In the limit of small Reynolds number $\mathcal{R}_e \ll 1$, the flow field resulting from a translating particle can be quite varied depending on the magnitude of the Taylor number (Greenspan 1968). For $\mathcal{T} \ll 1$ viscous forces dominate Coriolis forces, and the motion is approximately a Stokes flow with a superimposed swirling motion. In the geostrophic limit for which $\mathcal{T} \gg 1$, fluid motion in the lateral plane is not coupled with motion parallel to the rotation axis – a theoretical result implied by the Taylor–Proudman theorem (e.g. Batchelor 1967). Experimental observations, first made by Taylor (1922, 1923), show that a slowly translating particle in a rapidly rotating fluid is accompanied by a fluid column which extends parallel to the rotation axis. These Taylor columns form when the convective acceleration is small. Pritchard (1969) investigated particle motion parallel to the rotation axis and demonstrated that a Taylor column forms in an unbounded fluid when the Rossby number $\mathcal{R}_o \equiv \mathcal{R}_e \mathcal{T}^{-1} < 0.7$.

Table 1 summarizes theoretical and numerical studies related to particle motion along the rotation axis of an unbounded fluid, for flows with small convective inertial influences. The research primarily focuses on determining the drag on the particle as a function of the Taylor number. The low- and high-Taylor-number asymptotic limits for the particle drag were first deduced by Childress (1964) and Stewartson (1952), respectively. Weisenborn (1985) used the ‘method of induced forces’ to determine the drag on a rigid sphere for arbitrary Taylor number and confirmed the Childress and Stewartson asymptotic results. Dennis, Ingham & Singh (1982) numerically calculated the drag on a rigid sphere for small but finite Taylor and Reynolds numbers.

Until recently, only limited details of the flow field accompanying axial particle motion were available. Moore & Saffman (1969), in a detailed study of the high-Taylor-number limit, developed scaling arguments for the velocity variations within the Ekman and Stewartson layers as well as throughout the Taylor column. Recently Vedensky & Ungarish (1994) used dual integral expressions to analyse the motion of a translating infinitely thin disc for arbitrary Taylor numbers. They determined the

flow field everywhere in the fluid and demonstrated that the Taylor column terminates with two large recirculating regions of 'trapped fluid' which are detached from the particle surface.

Maxworthy (1965, 1968, 1970) performed experimental investigations in the parameter regime relevant to our study. His results for the particle drag as a function of Taylor number are compared with our numerical simulations in figure 5. The results show good agreement at low Taylor number. There remains a small discrepancy at high Taylor numbers, as previous authors have reported. Maxworthy also described features of the flow field which are in qualitative agreement with the numerical results presented in this paper, as well as by Vedensky & Ungarish.

Two topics which are outside the scope of this paper, but related to slow particle motion through rotating fluids, are worthy of mention. Particle translation perpendicular to the rotation axis has been studied experimentally and theoretically; a good introduction is provided by Herron, Davis & Bretherton (1975). Axial particle motion in bounded systems at high Taylor numbers has been investigated by Moore & Saffman (1968, 1969) and Hocking, Moore & Walton (1979) for rigid particles and Bush, Stone & Bloxham (1993) for drops.

Particle motion parallel to the rotation axis is relevant to the modelling of the centrifugal separation of two-phase flows. The assumption of motion parallel to the rotation axis is not unduly restrictive, since centrifugal forces drive a lighter phase inward toward the rotation axis, while buoyancy forces cause a vertical motion parallel to the rotation axis. Often the drag on the suspended particles is assumed to be Stokes drag (Hsu 1981), which corresponds to the limit $\mathcal{F} = 0$. In fact, the actual drag may be much larger owing to the dynamical effects of rotation (see figure 5). For example, a rigid sphere translating along the axis of a rotating fluid experiences a drag that is approximately four times the Stokes drag for $\mathcal{F} = 5$ and ten times the Stokes drag for $\mathcal{F} = 20$. Similar effects may be expected for particles moving through strong swirling or vortical flows.

A Taylor-column flow structure extends the hydrodynamic influence of a particle to larger distances than that of a particle moving through a non-rotating fluid. This long-range influence may have a profound effect on the rheology of suspension flows in rotating fluids, even those of a dilute nature (Ungarish 1993). For example, a 1 mm radius particle suspended in water inside a high-speed centrifuge rotating at 20000 RPM generates a Taylor column extending more than 10 cm. The same particle in the Stokes flow limit disturbs the fluid to the same degree at distances of about 1 cm.

In this paper we introduce a theoretical and numerical framework for studying particle motion in rotating fluids. The formalism is applicable to multiple particle systems and drops. The governing equations and the integral equation solution are given in §2. The solution is specialized to axisymmetric problems and on-axis motions in §3. Section 4 studies the drag and flow field for translating spheres and prolate ellipsoids. Comparisons with existing analyses and experimental results are reported and discussed.

2. Integral equation representation

Consider the motion of a rigid particle in a fluid of density ρ and kinematic viscosity ν that is in solid-body rotation with angular velocity $\boldsymbol{\Omega}$. Let a represent a typical dimension of the particle which translates with velocity \mathbf{U}_p and rotates relative to the fluid with angular velocity $\boldsymbol{\Omega}_p$. The equations of motion can be non-

dimensionalized using $U_p = |U_p|$, a , a/U_p , and $\mu U_p/a$ as the characteristic scales for velocity, length, time and pressure, respectively. In this case, the governing equations for the dimensionless velocity and pressure fields, written relative to axes rotating with steady angular velocity Ω , are

$$\mathcal{R}_e \left(\frac{\partial \mathbf{u}}{\partial t} + \mathbf{u} \cdot \nabla \mathbf{u} \right) + 2\mathcal{T}\Omega \wedge \mathbf{u} = -\nabla p + \nabla^2 \mathbf{u} = \nabla \cdot \mathbf{T} \quad \text{and} \quad \nabla \cdot \mathbf{u} = 0, \quad (2.1)$$

where p denotes the dimensionless reduced pressure, which incorporates the centrifugal acceleration and gravitational body force, and the stress tensor is $\mathbf{T} \equiv -p\mathbf{I} + (\nabla \mathbf{u} + \nabla \mathbf{u}')$. The Reynolds and Taylor numbers are two dimensionless parameters which characterize particle motion in rotating fluids and are defined in (1.1).

Boundary conditions for the motion of the particle are

$$\mathbf{u}(\mathbf{x}) = \mathbf{U}_p + \Omega_p \wedge (\mathbf{x} - \mathbf{x}_c) \quad \text{for } \mathbf{x} \in S_p, \quad (2.2)$$

$$\mathbf{u}(\mathbf{x}) \rightarrow \mathbf{0} \quad \text{for } |\mathbf{x} - \mathbf{x}_c| \rightarrow \infty, \quad (2.3)$$

where \mathbf{x} is the position vector, \mathbf{x}_c locates the particle centre of mass, and S_p denotes the particle surface.

2.1. Integral equation solutions to the linearized equations

For sufficiently small particle Reynolds number $\mathcal{R}_e \ll 1$, the quasi-steady linear equations governing particle motion in a rotating viscous flow are

$$2\mathcal{T}\Omega \wedge \mathbf{u} = -\nabla p + \nabla^2 \mathbf{u} \quad \text{and} \quad \nabla \cdot \mathbf{u} = 0. \quad (2.4)$$

The three terms in the momentum equation represent a balance between the pressure gradient, Coriolis and viscous forces. The limit $\mathcal{T} \ll 1$ gives Stokes flow, while the limit $\mathcal{T} \gg 1$ yields the geostrophic equation $2\mathcal{T}\Omega \wedge \mathbf{u} = -\nabla p$. This latter limit gives rise to the Taylor–Proudman theorem $\Omega \cdot \nabla \mathbf{u} = \mathbf{0}$ (obtained by taking the curl of the geostrophic equation), which constrains axial variations of velocity and explains the formation of Taylor columns accompanying translating particles (e.g. Greenspan 1968).

The equations of motion (2.4) can be recast as an integral equation relating the fluid velocity to the velocity and traction on the surface(s) S bounding the fluid domain V . The boundary integral equation is derived in Appendix A and has the form

$$\left. \begin{array}{l} \xi \in V; \quad \mathbf{u}(\xi) \\ \xi \in S; \quad \frac{1}{2}\mathbf{u}(\xi) \\ \xi \notin V; \quad \mathbf{0} \end{array} \right\} = - \int_S [\mathbf{n} \cdot \mathbf{T}(\mathbf{x}) \cdot \mathbf{G}(\mathbf{x}|\xi; \mathcal{T}) - \mathbf{u}(\mathbf{x})\mathbf{n}(\mathbf{x}) \cdot \mathbf{H}(\mathbf{x}|\xi; \mathcal{T})] \, dS_x, \quad (2.5)$$

where \mathbf{n} is the unit normal directed into V , ξ is a field point, and \mathbf{x} denotes the integration variable as shown in figure 1. The kernels \mathbf{G} and \mathbf{H} describe the velocity and stress fields at \mathbf{x} resulting from a point force $\hat{\mathbf{e}}$ at ξ and are defined as

$$\hat{\mathbf{u}}(\mathbf{x}) = \mathbf{G}(\mathbf{x}|\xi; \mathcal{T}) \cdot \hat{\mathbf{e}} \quad \text{and} \quad \hat{\mathbf{T}}(\mathbf{x}) = \mathbf{H}(\mathbf{x}|\xi; \mathcal{T}) \cdot \hat{\mathbf{e}}. \quad (2.6)$$

The Green's functions, or fundamental solutions, \mathbf{G} and \mathbf{H} satisfy the point-forced *adjoint* system of equations to (2.4):

$$-2\mathcal{T}\Omega \wedge \hat{\mathbf{u}} = -\nabla \hat{p} + \nabla^2 \hat{\mathbf{u}} + \hat{\mathbf{e}} \delta(\mathbf{x} - \xi) \quad \text{and} \quad \nabla \cdot \hat{\mathbf{u}} = 0. \quad (2.7)$$

The sign change on the Coriolis term in equation (2.7) eliminates volume integrals which would otherwise appear in the development of the integral equation (2.5).

This formulation is similar to the well-studied Stokes flow problem (e.g. Youngren

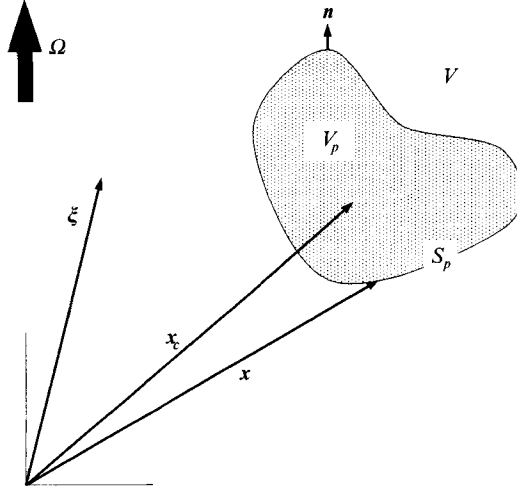


FIGURE 1. An arbitrary particle which is translating and rotating through a fluid in solid-body rotation with angular velocity Ω .

& Acrivos 1975; Kim & Karrila 1991; Pozrikidis 1992). The principal difference consists of the more complicated expressions for the rotating Green's functions \mathbf{G} and \mathbf{H} . These functions, which are valid for arbitrary Taylor number, are obtained by a Fourier transform of (2.7). For example,

$$\mathbf{G}(\mathbf{x}|\boldsymbol{\xi}; \mathcal{F}) = \frac{1}{8\pi^3} \int_{-\infty}^{\infty} \left[-\frac{2\mathcal{F}(\mathbf{k}\cdot\boldsymbol{\Omega})}{\Lambda} \mathbf{k}\cdot\boldsymbol{\epsilon} - \frac{(\mathbf{k}\cdot\mathbf{k})}{\Lambda} \mathbf{k}\mathbf{k} + \frac{(\mathbf{k}\cdot\mathbf{k})^2}{\Lambda} \mathbf{I} \right] e^{i\mathbf{k}\cdot(\mathbf{x}-\boldsymbol{\xi})} d\mathbf{k}, \quad (2.8)$$

where $\boldsymbol{\epsilon}$ is the third-rank permutation tensor and $\Lambda \equiv (\mathbf{k}\cdot\mathbf{k})^3 + 4\mathcal{F}^2(\mathbf{k}\cdot\boldsymbol{\Omega})^2$. A similar expression may be derived for $\mathbf{H}(\mathbf{x}|\boldsymbol{\xi}; \mathcal{F})$. Unfortunately, only two of the three inverse Fourier transformations can be deduced analytically; the remaining integration must be evaluated numerically (see § 3.2).

The functions \mathbf{G} and \mathbf{H} have the following properties. Setting $\mathcal{F} = 0$, the Green's function reduces to the Stokeslet solution

$$\mathbf{G} = \frac{1}{8\pi} \left(\frac{\mathbf{I}}{|\mathbf{r}|} + \frac{\mathbf{r}\mathbf{r}}{|\mathbf{r}|^3} \right) \text{ with } \mathbf{r} = \mathbf{x} - \boldsymbol{\xi}.$$

Interchanging source and receiver leads to the reciprocal property $G_{ij}(\mathbf{x}|\boldsymbol{\xi}; \mathcal{F}) = G_{ji}(\boldsymbol{\xi}|\mathbf{x}; -\mathcal{F})$, which is demonstrated in Appendix A. Symmetry of the stress tensor requires $H_{ijk} = H_{jik}$.

In the remainder of this paper we apply the boundary integral expression (2.5) to study the motion of a rigid particle translating along the rotation axis in an unbounded fluid.

2.2. Motion of a rigid particle

Applying the boundary conditions (2.2), (2.3) to the integral equation (2.5) yields a relationship between the velocity and surface traction on all bounding surfaces. Owing to the eventual viscous decay of the velocity field, the integral over the surface at infinity makes a vanishingly small contribution to (2.5). (In Appendix C we show that the velocity field within a conical region centred on the rotation axis decays as $(u, v, w) = O(r/z^2, (2\mathcal{F})^{1/3} r/z^{4/3}, 1/z)$. Outside of this conical region, numerical

evidence shows that the field decays at a faster rate.) The domain of the integral equation reduces to only the particle surface S_p and results in

$$\left. \begin{array}{l} \xi \in V; \quad \mathbf{u}(\xi) \\ \xi \in S_p; \quad \frac{1}{2} [\mathbf{U}_p + \boldsymbol{\Omega}_p \wedge (\xi - \mathbf{x}_c)] \\ \xi \notin V; \quad \mathbf{0} \end{array} \right\} - \int_{S_p} [\mathbf{U}_p + \boldsymbol{\Omega}_p \wedge (\mathbf{x} - \mathbf{x}_c)] \mathbf{n}(\mathbf{x}) : \mathbf{H}(\mathbf{x}|\xi; \mathcal{T}) dS_x \\ = - \int_{S_p} \mathbf{n} \cdot \mathbf{T}(\mathbf{x}) \cdot \mathbf{G}(\mathbf{x}|\xi; \mathcal{T}) dS_x. \quad (2.9)$$

The dependence on the third rank tensor \mathbf{H} may be eliminated by using the divergence theorem along with the identity $\nabla \cdot \mathbf{H} = -2\mathcal{T} \boldsymbol{\Omega} \wedge \mathbf{G} - \delta(\mathbf{x} - \xi)\mathbf{I}$, which follows from (2.6) and (2.7). We thus obtain

$$\left. \begin{array}{l} \xi \in V; \quad \mathbf{u}(\xi) \\ \xi \in S_p, V_p; \quad \mathbf{U}_p + \boldsymbol{\Omega}_p \wedge (\xi - \mathbf{x}_c) \end{array} \right\} - 2\mathcal{T} \int_{V_p} [\boldsymbol{\Omega} \wedge (\mathbf{U}_p + \boldsymbol{\Omega}_p \wedge (\mathbf{x} - \mathbf{x}_c))] \cdot \mathbf{G}(\mathbf{x}|\xi; \mathcal{T}) dV_x \\ = - \int_{S_p} \mathbf{n} \cdot \mathbf{T}(\mathbf{x}) \cdot \mathbf{G}(\mathbf{x}|\xi; \mathcal{T}) dS_x. \quad (2.10)$$

Here V_p denotes the particle volume. The net force and torque exerted by the fluid on the particle are given by

$$\mathbf{F}^H = \int_{S_p} \mathbf{n} \cdot \mathbf{T}(\mathbf{x}) dS_x \quad \text{and} \quad \mathbf{L}^H = \int_{S_p} (\mathbf{x} - \mathbf{x}_c) \wedge \mathbf{n} \cdot \mathbf{T}(\mathbf{x}) dS_x. \quad (2.11)$$

The integral expressions (2.9) or (2.10), subject to the possible constraints imposed by the net force and/or torque (2.11), form the starting point for the numerical study of low-Reynolds-number rigid particle motions in rotating fluids. The problem may be stated in a number of ways: (i) given the particle translational velocity \mathbf{U}_p and rotational velocity $\boldsymbol{\Omega}_p$, determine the surface traction $\mathbf{n} \cdot \mathbf{T}$ and hence the force \mathbf{F}^H and torque \mathbf{L}^H causing the motion; (ii) given the translational velocity of a torque-free particle, determine the surface traction and rotational velocity; (iii) given the net force and torque, determine the velocity and rotation rate.

For any of the problems mentioned above, the integral expression (2.9) or (2.10) for $\xi \in S_p$, together with the auxiliary conditions on net force and torque (2.11), specify a well-posed boundary-value problem. The velocity field at any point in the fluid domain ($\xi \in V$) may be calculated from (2.9) or (2.10) once the surface traction and velocity have been determined.

In this paper we assume that the particle does not rotate ($\boldsymbol{\Omega}_p = \mathbf{0}$) and translates with prescribed velocity \mathbf{U}_p in a direction parallel to the rotation axis ($\mathbf{U}_p \wedge \boldsymbol{\Omega} = \mathbf{0}$). The volume integral in (2.10) thus vanishes and the integral equation simplifies to

$$\left. \begin{array}{l} \xi \in V; \quad \mathbf{u}(\xi) \\ \xi \in S_p, V_p; \quad \mathbf{U}_p \end{array} \right\} = - \int_{S_p} \mathbf{n} \cdot \mathbf{T}(\mathbf{x}) \cdot \mathbf{G}(\mathbf{x}|\xi; \mathcal{T}) dS_x. \quad (2.12)$$

By restricting $\xi \in S_p$, equation (2.12) is an integral equation of the first kind to be solved for the unknown surface traction $\mathbf{n} \cdot \mathbf{T}$.

The assumption of translation without rotation is not unduly restrictive. A torque-free, axisymmetric, fore-aft symmetric particle, translating along the rotation axis of an unbounded fluid, does not rotate relative to the fluid, although oppositely directed swirl velocities are generated fore and aft of the particle. This motion is a consequence of the symmetry of the governing linear equations. Breaking fore-aft symmetry, by

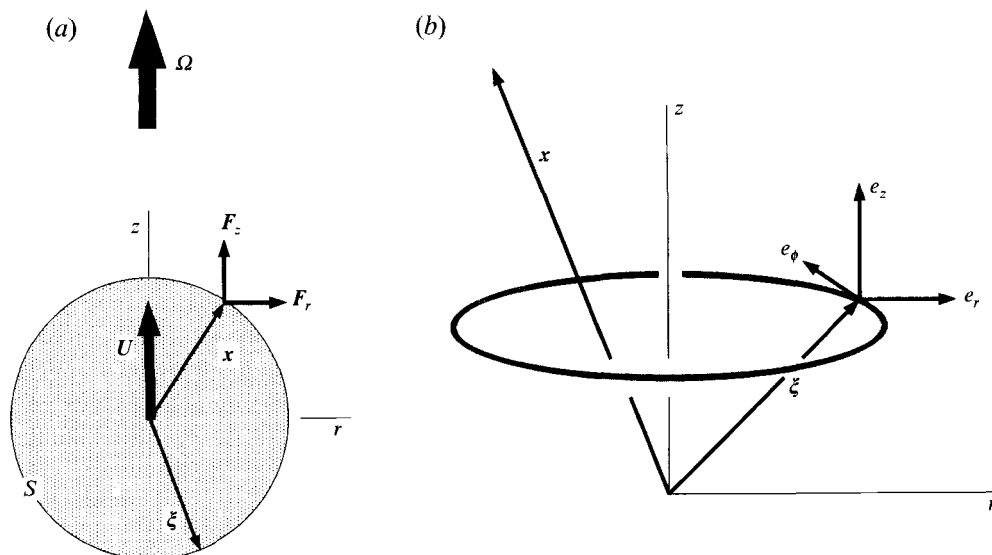


FIGURE 2. (a) Axisymmetric particle translating along the rotation axis. (b) Ring of point forces passing through ξ with the field point at x .

either altering the particle geometry or by including boundaries, will cause the particle to undergo relative rotation. In a future study, we will use the representation (2.9) or (2.10) to examine such problems. The next section considers simplifications associated with axial symmetry.

3. Axisymmetric Green's function

The integral equation (2.12) relating the surface velocity and tractions is unwieldy to solve because five integral evaluations are required: two over the physical space variables describing the particle surface and three over the Fourier space variables defining the Green's function. However, for axially symmetric flows, three integrations may be performed analytically, thereby rendering a significant simplification.

Using cylindrical coordinates (r, ϕ, z) with position vectors $x = (r, z)$, $\xi = (\eta, \zeta)$ as shown in figure 2a, and denoting the axisymmetric velocity field $u = (u, v, w)$, the integral equation (2.12) describing translation of an axisymmetric rigid particle along the rotation axis may be written

$$u(\xi) = - \int_s 2\pi r \mathbf{F} \cdot \mathbf{M}(x|\xi; \mathcal{F}) ds_x, \tag{3.1}$$

where the arclength s is the trace of the particle boundary in the (r, z) plane and $\mathbf{F} = (F_r, F_\phi, F_z)$ is the local surface traction vector expressed in cylindrical coordinates. The details of this simplification are presented in §§ 3.1 and 3.2, but a few introductory remarks are helpful.

The second-rank tensor $\mathbf{M}(x|\xi; \mathcal{F})$ is the axisymmetric analogue of the Green's function \mathbf{G} and involves a single integral evaluation (see (3.22)). \mathbf{M} describes the (axisymmetric) adjoint velocity \hat{u} at field point x , which arises from an axisymmetric ring force $\hat{e} = (\hat{e}_r, \hat{e}_\phi, \hat{e}_z)$ passing through ξ , as illustrated in figure 2b:

$$\hat{u}(x) = \mathbf{M}(x|\xi; \mathcal{F}) \cdot \hat{e}(\xi). \tag{3.2}$$

Owing to the sign change on the Coriolis term in the adjoint equation, care must be exercised in drawing a physical interpretation, since the direction of certain components of $\hat{\mathbf{u}}$ may be opposite from that expected from a given forcing.

For later use, we define the components in \mathbf{M} using the notation

$$\mathbf{M}(\mathbf{x}|\xi; \mathcal{F}) = \begin{bmatrix} M_{rr} & M_{r\phi} & M_{rz} \\ M_{\phi r} & M_{\phi\phi} & M_{\phi z} \\ M_{zr} & M_{z\phi} & M_{zz} \end{bmatrix} (\mathbf{x}|\xi; \mathcal{F}). \quad (3.3)$$

The next three subsections provide details of the axisymmetric formulation. Section 3.1 presents two methods for eliminating the azimuthal dependence and so establishes the axisymmetric Green's function \mathbf{M} . The first method directly determines \mathbf{M} from the axisymmetric form of the governing equations. Setting $\mathcal{F} = 0$, we arrive at a novel way of determining the axisymmetric Stokes flow Green's function and associated pressure field. The second method employs techniques from the Stokes flow literature (e.g. Pozrikidis 1992) whereby the original integral expression is integrated along the azimuthal direction. Both methods lead to identical integral representations of the Green's function, which involves inverse transforms along the axial and radial directions. In §3.2 residue theory is used to evaluate the axial integration, thereby reducing the Green's function to a single integration. Section 3.3 provides details of the numerical implementation and §3.4 concludes by examining the response to a point force located at the origin.

3.1. Eliminate azimuthal dependence

3.1.1. Impose axial symmetry on the governing equations

The axisymmetric form of the integral equation (3.1) may be formally developed as outlined in Appendix A. Equation (3.1) utilizes the Green's function \mathbf{M} which satisfies the axisymmetric form of the adjoint equation subject to a ring of point forces.

Defining the adjoint velocity to be $\hat{\mathbf{u}} = (\hat{u}, \hat{v}, \hat{w})$ and the axisymmetric components of the ring force through the point ξ to be $\hat{\mathbf{e}} = (\hat{e}_r, \hat{e}_\phi, \hat{e}_z)$, the governing equations (2.7) may be written

$$2\mathcal{F}\hat{v} = -\frac{\partial\hat{p}}{\partial r} + \frac{\partial^2\hat{u}}{\partial r^2} + \frac{1}{r}\frac{\partial\hat{u}}{\partial r} - \frac{\hat{u}}{r^2} + \frac{\partial^2\hat{u}}{\partial z^2} + \frac{\hat{e}_r}{2\pi\eta} \delta(r-\eta) \delta(z-\zeta), \quad (3.4)$$

$$-2\mathcal{F}\hat{u} = \frac{\partial^2\hat{v}}{\partial r^2} + \frac{1}{r}\frac{\partial\hat{v}}{\partial r} - \frac{\hat{v}}{r^2} + \frac{\partial^2\hat{v}}{\partial z^2} + \frac{\hat{e}_\phi}{2\pi\eta} \delta(r-\eta) \delta(z-\zeta), \quad (3.5)$$

$$0 = -\frac{\partial\hat{p}}{\partial z} + \frac{\partial^2\hat{w}}{\partial r^2} + \frac{1}{r}\frac{\partial\hat{w}}{\partial r} + \frac{\partial^2\hat{w}}{\partial z^2} + \frac{\hat{e}_z}{2\pi\eta} \delta(r-\eta) \delta(z-\zeta), \quad (3.6)$$

$$0 = \frac{1}{r}\frac{\partial}{\partial r}(r\hat{u}) + \frac{\partial\hat{w}}{\partial z}, \quad (3.7)$$

where the three-dimensional delta function has been expressed as a ring forcing using $\delta(\mathbf{x}-\xi) = \delta(r-\eta) \delta(z-\zeta) / (2\pi\eta)$.

These equations are solved by applying a Fourier transform in z , and a Hankel

transform of order 1 to equations (3.4) and (3.5) and of order 0 to equations (3.6) and (3.7). The transform variables (U, V, W, P) with wavenumber vectors (k, n) are defined as

$$\begin{pmatrix} U(k, n) \\ V(k, n) \end{pmatrix} = \int_0^\infty \int_{-\infty}^\infty r \begin{pmatrix} \hat{u}(r, z) \\ \hat{v}(r, z) \end{pmatrix} J_1(rk) e^{-inz} dz dr \quad (3.8)$$

and

$$\begin{pmatrix} W(k, n) \\ P(k, n) \end{pmatrix} = \int_0^\infty \int_{-\infty}^\infty r \begin{pmatrix} \hat{w}(r, z) \\ \hat{p}(r, z) \end{pmatrix} J_0(rk) e^{-inz} dz dr, \quad (3.9)$$

with the complementary inversion formulae

$$\begin{pmatrix} \hat{u}(r, z) \\ \hat{v}(r, z) \end{pmatrix} = \frac{1}{2\pi} \int_0^\infty \int_{-\infty}^\infty k \begin{pmatrix} U(k, n) \\ V(k, n) \end{pmatrix} J_1(rk) e^{inz} dn dk \quad (3.10)$$

and

$$\begin{pmatrix} \hat{w}(r, z) \\ \hat{p}(r, z) \end{pmatrix} = \frac{1}{2\pi} \int_0^\infty \int_{-\infty}^\infty k \begin{pmatrix} W(k, n) \\ P(k, n) \end{pmatrix} J_0(rk) e^{inz} dn dk. \quad (3.11)$$

The transforms (e.g. Sneddon 1972) reduce equations (3.4)–(3.7) to four algebraic expressions, which are straightforward to solve:

$$[U, V, W, P]^t = \frac{e^{-in\zeta}}{2\pi A} \times \begin{bmatrix} n^2(k^2+n^2) J_1(\eta k) & -2\mathcal{F} n^2 J_1(\eta k) & -ink(n^2+k^2) J_0(\eta k) \\ 2\mathcal{F} n^2 J_1(\eta k) & (k^2+n^2)^2 J_1(\eta k) & -i2\mathcal{F} nk J_0(\eta k) \\ ink(k^2+n^2) J_1(\eta k) & -i2\mathcal{F} nk J_1(\eta k) & k^2(n^2+k^2) J_0(\eta k) \\ -k(k^2+n^2)^2 J_1(\eta k) & 2\mathcal{F} k(k^2+n^2) J_1(\eta k) & -in(4\mathcal{F}^2+(n^2+k^2)^2) J_0(\eta k) \end{bmatrix} \cdot \begin{bmatrix} \hat{e}_r \\ \hat{e}_\phi \\ \hat{e}_z \end{bmatrix}, \quad (3.12)$$

where

$$A \equiv (k^2 + n^2)^3 + 4\mathcal{F}^2 n^2. \quad (3.13)$$

Explicitly writing the inverse transforms, the axisymmetric form of the Green's function \mathbf{M} may be expressed compactly in the form

$$\mathbf{M}(r, z|\eta, \zeta; \mathcal{F}) = \int_0^\infty \int_{-\infty}^\infty dk dn \frac{k e^{in(z-\zeta)}}{4\pi^2 A} \times \begin{bmatrix} n^2(k^2+n^2)J_1(kr)J_1(k\eta) & -2\mathcal{F} n^2 J_1(kr)J_1(k\eta) & -ink(k^2+n^2)J_1(kr)J_0(k\eta) \\ 2\mathcal{F} n^2 J_1(kr)J_1(k\eta) & (k^2+n^2)^2 J_1(kr)J_1(k\eta) & -i2\mathcal{F} kn J_1(kr)J_0(k\eta) \\ ink(k^2+n^2)J_0(kr)J_1(k\eta) & -i2\mathcal{F} nk J_0(kr)J_1(k\eta) & k^2(k^2+n^2)J_0(kr)J_0(k\eta) \end{bmatrix}, \quad (3.14)$$

where the components of \mathbf{M} correspond to equation (3.3).

Before proceeding with further details of the inverse transform, we explicitly demonstrate the relationship between the axisymmetric function $\mathbf{M}(\mathbf{x}|\xi; \mathcal{T})$ and the original Green's function $\mathbf{G}(\mathbf{x}|\xi; \mathcal{T})$.

3.1.2. Azimuthal integration of \mathbf{G}

An alternative method for deriving \mathbf{M} is to integrate equation (2.5) along the azimuthal direction. This procedure is standard for axisymmetric Stokes flow problems (e.g. Pozrikidis 1992). We provide a few details since the intermediate steps are altered owing to the more complicated form of the governing equations for rotating viscous flow.

We introduce a cylindrical coordinate system with position vectors $\xi = (\eta, 0, \zeta)$ and $\mathbf{x} = (r \cos \phi, r \sin \phi, z)$, and denote the area element as $dS_x = r d\phi ds$, where s denotes a differential element of arclength along the surface. The surface traction is independent of the azimuthal coordinate, and is written relative to the Cartesian coordinate system as

$$\mathbf{n} \cdot \mathbf{T} = (F_r \cos \phi - F_\phi \sin \phi, F_r \sin \phi + F_\phi \cos \phi, F_z). \quad (3.15)$$

The general boundary integral expression (2.5) may be rearranged to yield

$$\begin{aligned} \mathbf{u}(\xi) = & \int_s \mathbf{F} \cdot \int_0^{2\pi} \begin{bmatrix} G_{11} \cos \phi + G_{21} \sin \phi & G_{12} \cos \phi + G_{22} \sin \phi & G_{13} \cos \phi + G_{23} \sin \phi \\ G_{21} \cos \phi - G_{11} \sin \phi & G_{22} \cos \phi - G_{12} \sin \phi & G_{23} \cos \phi - G_{13} \sin \phi \\ G_{31} & G_{32} & G_{33} \end{bmatrix} \\ & \times r d\phi ds, \end{aligned} \quad (3.16)$$

where the surface traction vector is $\mathbf{F} = (F_r, F_\phi, F_z)$ and the components of the Green's function G_{ij} are given in equation (2.8) in terms of a Fourier inversion. Equation (3.16) involves five integrations: two over physical space variables and three over Fourier space variables.

The Fourier inversion integral (2.8) may be simplified using cylindrical coordinates with the wavenumber vector defined as $\mathbf{k} = (k \cos \phi', k \sin \phi', n)$, so that $\mathbf{k} \cdot (\mathbf{x} - \xi) = rk \cos(\phi - \phi') - \eta k \cos \phi' + n(z - \zeta)$ and $d\mathbf{k} = k d\phi' dk dn$. The two angular integrations (ϕ, ϕ') have closed-form solutions obtained using the identities

$$\int_0^{2\pi} \cos(m\phi') e^{i t \cos \phi'} d\phi' = 2\pi i^m J_m(t), \quad (3.17)$$

where $J_m(t)$ is the Bessel function of the first kind of order m (Morse & Feshbach 1953), and

$$\int_0^{2\pi} \begin{pmatrix} \sin \phi \\ \cos \phi \end{pmatrix} e^{i k r \cos(\phi - \phi')} d\phi = \begin{pmatrix} \sin \phi' \\ \cos \phi' \end{pmatrix} 2\pi i J_1(kr), \quad (3.18)$$

which follows from (3.17) with a change of variables. Performing the two azimuthal integrations in (3.16) leads directly to the axisymmetric form of the integral equation (3.1) and the function \mathbf{M} given in (3.14).

3.2. The axial inverse transform

The integral over the axial wavenumber n is evaluated using contour integration. Simple poles of the integrand of equation (3.14) occur where

$$A = (n^2 + k^2)^3 + 4\mathcal{T}^2 n^2 \equiv (n^2 + c^2)(n^2 - N^2)(n^2 - \overline{N^2}) = 0. \quad (3.19)$$

The roots of this cubic equation for n^2 are expressed in terms of

$$c^2 = k^2 - (s_1 + s_2) \quad \text{and} \quad 2N^2 = -(s_1 + s_2 + 2k^2) + i\sqrt{3}(s_1 - s_2), \quad (3.20)$$

where $c^2 \geq 0$ for all k , $\overline{N^2}$ represents the complex conjugate of N^2 , and

$$s_1 = \left[2\mathcal{F}^2 \left((k^4 + \frac{16}{27}\mathcal{F}^2)^{1/2} + k^2 \right) \right]^{1/3}, \quad s_2 = - \left[2\mathcal{F}^2 \left((k^4 + \frac{16}{27}\mathcal{F}^2)^{1/2} - k^2 \right) \right]^{1/3}. \quad (3.21)$$

The three roots are distinct for $\mathcal{F} \neq 0$. In the limit $\mathcal{F} = 0$, the roots form a triple pole at $n^2 = -k^2$.

For $z - \zeta \geq 0$ and $\mathcal{F} \neq 0$, the contour integral is closed in the upper half-plane and the residue evaluated for simple poles $n = ic, N$ and $-\overline{N}$. For $z - \zeta < 0$, the contour is closed in the lower half-plane with poles $n = -ic, -N$ and \overline{N} . Performing the contour integration, the components of \mathbf{M} are

$$M_{rr} = \frac{1}{2\pi} \int_0^\infty k \left[-\frac{c(k^2 - c^2)}{A_1} e^{-c|z-\zeta|} + 2\text{Re} \left\{ \frac{iN(k^2 + N^2)}{A_2} e^{iN|z-\zeta|} \right\} \right] J_1(kr)J_1(k\eta) dk, \quad (3.22a)$$

$$M_{r\phi} = \frac{-2\mathcal{F}}{2\pi} \int_0^\infty k \left[-\frac{c}{A_1} e^{-c|z-\zeta|} + 2\text{Re} \left\{ \frac{iN}{A_2} e^{iN|z-\zeta|} \right\} \right] J_1(kr)J_1(k\eta) dk, \quad (3.22b)$$

$$M_{rz} = \frac{\text{sgn}(z - \zeta)}{2\pi} \int_0^\infty k^2 \left[\frac{k^2 - c^2}{A_1} e^{-c|z-\zeta|} + 2\text{Re} \left\{ \frac{k^2 + N^2}{A_2} e^{iN|z-\zeta|} \right\} \right] J_1(kr)J_0(k\eta) dk, \quad (3.22c)$$

$$M_{\phi r} = \frac{2\mathcal{F}}{2\pi} \int_0^\infty k \left[-\frac{c}{A_1} e^{-c|z-\zeta|} + 2\text{Re} \left\{ \frac{iN}{A_2} e^{iN|z-\zeta|} \right\} \right] J_1(kr)J_1(k\eta) dk, \quad (3.22d)$$

$$M_{\phi\phi} = \frac{1}{2\pi} \int_0^\infty k \left[\frac{(k^2 - c^2)^2}{cA_1} e^{-c|z-\zeta|} + 2\text{Re} \left\{ \frac{i(k^2 + N^2)^2}{NA_2} e^{iN|z-\zeta|} \right\} \right] J_1(kr)J_1(k\eta) dk, \quad (3.22e)$$

$$M_{\phi z} = \frac{\text{sgn}(z - \zeta)2\mathcal{F}}{2\pi} \int_0^\infty k^2 \left[\frac{1}{A_1} e^{-c|z-\zeta|} + 2\text{Re} \left\{ \frac{1}{A_2} e^{iN|z-\zeta|} \right\} \right] J_1(kr)J_0(k\eta) dk, \quad (3.22f)$$

$$M_{zr} = \frac{-\text{sgn}(z - \zeta)}{2\pi} \int_0^\infty k^2 \left[\frac{k^2 - c^2}{A_1} e^{-c|z-\zeta|} + 2\text{Re} \left\{ \frac{k^2 + N^2}{A_2} e^{iN|z-\zeta|} \right\} \right] J_0(kr)J_1(k\eta) dk, \quad (3.22g)$$

$$M_{z\phi} = \frac{\text{sgn}(z - \zeta)2\mathcal{F}}{2\pi} \int_0^\infty k^2 \left[\frac{1}{A_1} e^{-c|z-\zeta|} + 2\text{Re} \left\{ \frac{1}{A_2} e^{iN|z-\zeta|} \right\} \right] J_0(kr)J_1(k\eta) dk, \quad (3.22h)$$

$$M_{zz} = \frac{1}{2\pi} \int_0^\infty k^3 \left[\frac{k^2 - c^2}{cA_1} e^{-c|z-\zeta|} + 2\text{Re} \left\{ \frac{i(k^2 + N^2)}{NA_2} e^{iN|z-\zeta|} \right\} \right] J_0(kr)J_0(k\eta) dk, \quad (3.22i)$$

where Re specifies the real part, sgn takes the sign of the argument, and

$$A_1 \equiv 2(c^2 + N^2)(c^2 + \overline{N^2}) \quad \text{and} \quad A_2 \equiv 2(c^2 + N^2)(N^2 - \overline{N^2}). \quad (3.23)$$

No further analytical simplifications of these expressions are possible.

3.3. Numerical implementation

We begin with a few observations relevant to the numerical evaluation of (3.22) and solution of (3.1). The Stokes flow response (or Stokeslet) corresponds to setting

$\mathcal{T} = 0$, so that equation (3.14) reduces to

$$\mathbf{M}^{Stokes} = \int_0^\infty \int_{-\infty}^\infty dk dn \frac{ke^{in(z-\zeta)}}{4\pi^2(k^2 + n^2)^2} \times \begin{bmatrix} n^2 J_1(kr)J_1(k\eta) & 0 & -inkJ_1(kr)J_0(k\eta) \\ 0 & (k^2 + n^2)J_1(kr)J_1(k\eta) & 0 \\ inkJ_0(kr)J_1(k\eta) & 0 & k^2 J_0(kr)J_0(k\eta) \end{bmatrix}. \quad (3.24)$$

In Appendix B we show how to recover the common form of the Stokeslet which involves elliptic integrals. The components in (3.24) which are identically zero indicate that the swirling motion is decoupled from the axial and radial motions in the limit $\mathcal{T} = 0$. This decoupling no longer holds when rotational effects are included. Axisymmetric flows at finite Taylor numbers have swirling motions caused by axial and radial surface forces, as well as axial and radial fluid motions caused by azimuthal surface forces.

Although not obvious from the form of (3.22), the diagonal terms $M_{rr}, M_{\phi\phi}$ and M_{zz} are logarithmically singular as $\mathbf{x} \rightarrow \boldsymbol{\xi}$ (as in the Stokes flow limit). The other components of \mathbf{M} are non-singular. From a numerical standpoint, it is convenient to remove the singularity, so that integrals are ‘well behaved’ in the vicinity of the singularity. In Appendix B we introduce the disturbance Green’s function defined by subtracting the singular Stokeslet $\mathbf{M}^d = \mathbf{M} - \mathbf{M}^{Stokes}$; then \mathbf{M}^d is non-singular everywhere.

The explicit dependence on the Taylor number in the denominator of \mathbf{M} may be eliminated by suitably rescaling lengths. In particular, the Green’s function satisfies

$$\mathbf{M}(r, z|\eta, \zeta; \mathcal{T}) = \mathcal{T}^{1/2} \mathbf{M}(\mathcal{T}^{1/2}r, \mathcal{T}^{1/2}z|\mathcal{T}^{1/2}\eta, \mathcal{T}^{1/2}\zeta; 1). \quad (3.25)$$

This rescaling has numerical advantages over the unscaled equation by keeping terms $O(1)$ in the integrand of the Green’s function and has been used in the calculations reported here. The reciprocity relation $M_{ij}(r, z|\eta, \zeta; \mathcal{T}) = M_{ji}(\eta, \zeta|r, z; -\mathcal{T})$ can be demonstrated by direct substitution. This identity may be helpful for reducing the computation time in more complex problems, although we have not yet tried to implement this idea.

We attempted various solution strategies for numerically evaluating the Green’s function (3.22) accurately and quickly. These strategies included: (i) direct integration of the Green’s function (3.22); (ii) removing the singular Stokeslet, integrating the disturbance function \mathbf{M}^d , and then adding the Stokeslet using its analytic representation (see Appendix B for details); (iii) developing asymptotic expressions valid for $\mathcal{T}^{1/2}|z - \zeta| \gg 1$. Details of the asymptotic approximations appear in Appendix C.

The IMSL routine DQDAGI (adaptive Gauss quadrature for an infinite integration range) was used to perform the integrations with the error criteria typically chosen as $ERRABS = ERRREL = 10^{-4}$. Convergence of the integrations was difficult for large values of the Taylor number ($\mathcal{T} > 10^4$) and/or large distances.

Method (ii) was most efficient for solving the integral equation to obtain the surface tractions, and a combination of methods (i) and (iii) was best for determining velocity fields. Computations were performed using a Sun Sparc 1+ workstation and the times required to calculate all of the Green’s function components at 60 (r, z) locations for a fixed (η, ζ) are summarized below.

For (r, z) along a unit sphere and $(\eta, \zeta) = (\sqrt{2}/2, \sqrt{2}/2)$, chosen since it is represen-

tative of typical calculations involved in solving the integral equation:

$$\mathbf{M} \approx 115 \text{ s}, \quad \mathbf{M}^{dist} + \mathbf{M}^{Stokes} \approx 54 \text{ s}.$$

For (r, z) along the line $(0, 0) - (3, 30)$, with $(\eta, \zeta) = (1, 0)$, which simulates a typical calculation of the velocity field:

$$\mathbf{M} \approx 27 \text{ s}, \quad \mathbf{M}^{dist} + \mathbf{M}^{Stokes} \approx 45 \text{ s}, \quad \mathbf{M}^{asym} \approx 11 \text{ s}.$$

In the far field, it is better to calculate the total Green's function or the asymptotic approximation. The asymptotic expressions had an absolute error less than 10^{-4} when $\mathcal{F}^{1/2}|z - \zeta| > 10$.

(Since the initial submission of this article, Lucas 1994 has developed more efficient and accurate quadrature schemes for evaluating \mathbf{M} .)

3.4. Response to a point force at the origin

We conclude our discussion of the Green's function by considering the flow resulting from an axial point force of strength F located at the origin. Since there is no geometric lengthscale in this example, the equations of motion are non-dimensionalized using the Ekman length $(\nu/\Omega)^{1/2}$ and the characteristic velocity $F\Omega^{1/2}/(\rho\nu^{3/2})$. This scaling corresponds to setting $\mathcal{F} = 1$ in the equations of motion.

Figure 3(a) shows the streamlines projected onto the (r, z) -plane, and figure 3(b) shows contours of the induced swirling flow v/r . The streamlines are closed, in contrast to the familiar streamlines for a Stokeslet. The Coriolis force induces oppositely directed swirls up- and downstream of the forcing, with fluid rotating slower than the bulk in front of the forcing, and faster than the bulk behind the forcing.

Near the origin the flow in the (r, z) -plane qualitatively resembles that due to a Stokeslet; farther away, the flow is dominated by the rotational effects which create a weak return (down) flow ($w < 0$). From the numerical solution, the stagnation point $\mathbf{u}(r_0^*, z_0^*) = 0$ was found to be $(1.7371 < r_0^* < 1.7372, z_0^* = 0)$ which is almost, but not quite, at a radial location $\sqrt{3}$.

Rotational effects suppress radial motions and smooth out axial variations, producing an elongated or conical structure to the flow field. We illustrate this qualitative feature of the flow with the dotted line in figure 3, which is the locus of points where the axial component of the flow changes direction, i.e. $w(r^*, z^*) = 0$. This structure scales as $r/z^{1/3} = \text{constant}$, a result suggested by the far-field asymptotic analysis developed in Appendix C.

Finally, the velocity field far from the forcing $z \gg 1$ and located within a cone $r/z^{1/3} \ll 1$, may be shown analytically to decay like

$$u \approx \frac{r}{z^2}, \quad v \approx -\frac{r}{z^{4/3}}, \quad w \approx \frac{1}{z}. \quad (3.26)$$

Numerical results have verified this dependence.

4. Numerical results for axial particle motion

We present detailed numerical results for the translation of a rigid axisymmetric particle parallel to the rotation axis in an unbounded fluid. The surface stress distribution, total force acting on the particle, and the detailed velocity field are determined for a sphere (§4.1) and a family of prolate spheroids (§4.2) for $0 \leq \mathcal{F} < 10^4$. Our drag calculations for a translating sphere agree with analytical results

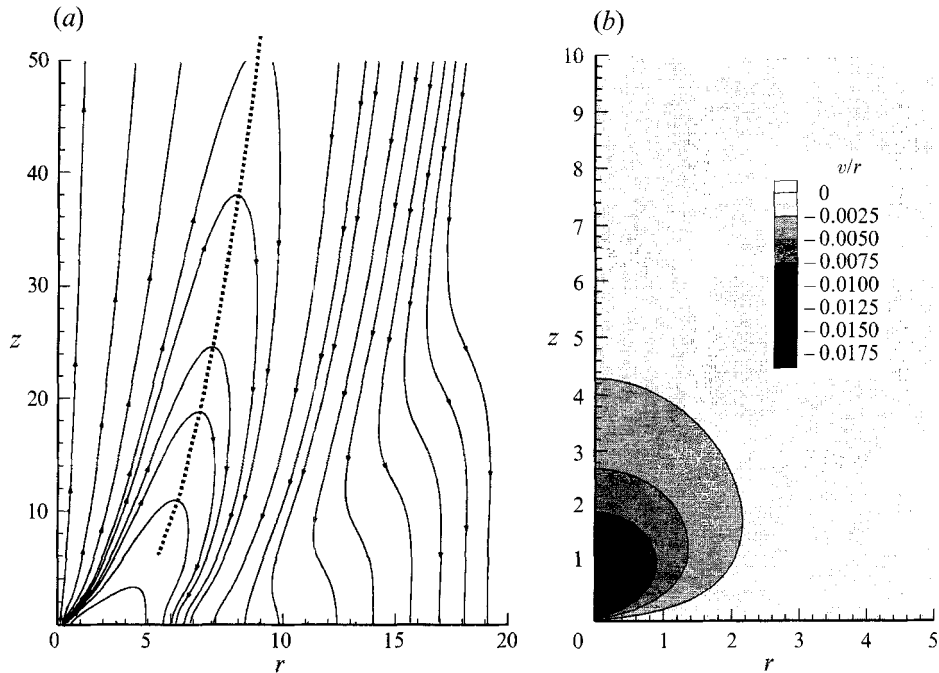


FIGURE 3. Velocity field arising from a point force $F\hat{e}_z$ located at the origin: (a) streamlines projected onto the (r, z) -plane, (b) contours of the swirl angular velocity v/r . The dotted line in (a) passes through $w(r^*, z^*) = 0$ and illustrates a flow structure scaling as $r/z^{1/3} = \text{constant}$.

known in the high- and low-Taylor-number limits, and with the analytical results of Weisenborn (1985) which span all Taylor numbers. Additionally for $\mathcal{T} > 50$, the velocity field shows a truncated Taylor column bounded by detached recirculating regions. Vedensky & Ungarish (1994) described a similar flow feature associated with the axial translation of a rigid disc. Section 4.2 investigates the translation of prolate spheroids and examines the effect that the particle shape has on the drag.

We solve the integral equation of the first kind (3.1), using the method of Kantorovich & Krylov (e.g. Youngren & Acrivos 1975) whereby the surface is subdivided into N equal sections and the unknown stress distribution \mathbf{F} is assumed constant over a given section. The integral equation reduces to a set of $3N$ algebraic equations, which are solved using standard matrix methods to obtain the stress distribution. The symmetry of fore-aft axisymmetric particles allows the unknown tractions to be limited to the first quadrant of the particle surface.

To demonstrate the convergence of the numerical method, we present typical results for the surface traction as the number of surface subdivisions is increased. Figure 4 shows the calculated azimuthal stress component F_ϕ as a function of angular position θ (see figure 6) at $\mathcal{T} = 500$ for three different subdivisions. Table 2 presents values of the surface traction for $N = 15, 31, 51$ at locations $\theta = 0.3\pi$ and 0.5π (equator). The differences in the stress distributions between the $N = 31$ and $N = 51$ simulations are less than 1% for all θ . The calculations presented below typically used $N = 51$ elements.

We encountered numerical difficulties for $\mathcal{T} > 10^4$ due to excessive roundoff error in the Green's function calculation. We suspect this problem could be alleviated by rescaling the surface tractions to keep them $O(1)$ as the Taylor number is increased,

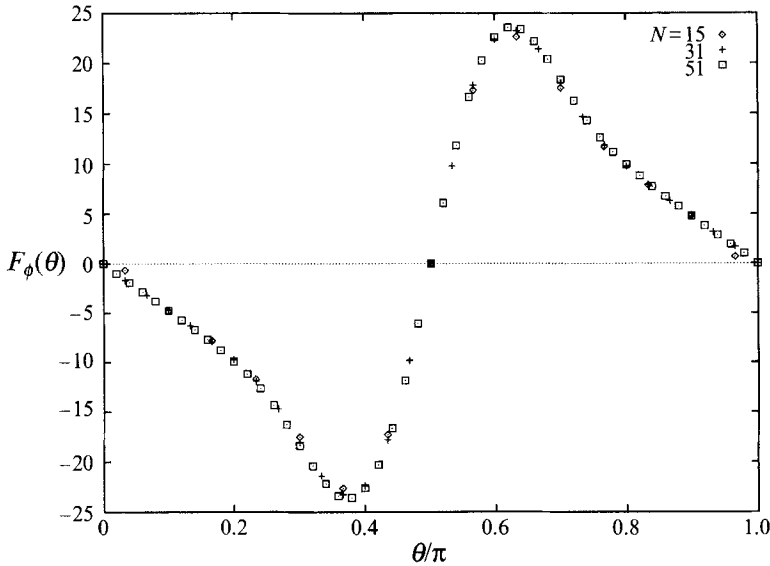


FIGURE 4. Surface traction F_ϕ on a rigid sphere ($\mathcal{T} = 500$). These results demonstrate the convergence of the numerical solution as the number of elements N increases. The angular position θ is measured from the z axis (see figure 6). The difference in stress distribution between $N = 31$ and $N = 51$ is less than 1% for all θ .

N	$F_r(\theta = 0.3\pi)$	$F_\phi(\theta = 0.3\pi)$	$F_z(\theta = 0.3\pi)$	$F_z(\theta = 0.5\pi)$
15	291.38	17.52	230.40	52.66
31	295.03	18.17	233.41	53.68
51	296.23	18.36	234.47	53.97

TABLE 2. Components of the surface traction for a translating sphere ($\mathcal{T} = 500$). The magnitude of the components are shown at two positions $\theta = 0.3\pi$ and 0.5π (see figure 6) for increasing number of elements $N = 15, 31, 51$.

by expressing the unknown surface tractions in terms of normal and tangential components, or by improving the numerical quadrature scheme used to calculate the Green's function. (In the period following acceptance of this article, Lucas 1994 developed more accurate and efficient numerical quadrature routines which directly incorporate Bessel function kernels. These new routines have allowed us to extend the Green's function calculations to Taylor number $\mathcal{T} > 10^4$.)

4.1. Rigid sphere

This section presents results for a rigid sphere translating parallel to the rotation axis. A plot of the dimensionless drag $D(\mathcal{T}) = |\mathbf{F}^H|$ normalized relative to the dimensionless Stokes drag 6π is shown in figure 5. The figure includes the asymptotic approximations of Childress ($D/6\pi = 1 + 4\mathcal{T}/7$ for $\mathcal{T} \ll 1$) and Stewartson ($D/6\pi = 8\mathcal{T}/9\pi$ for $\mathcal{T} \gg 1$). Weisenborn (1985) used a multipole method to obtain the drag for arbitrary Taylor number and reported the following improvement to the low-Taylor-number expansion:

$$\frac{D}{6\pi} \approx 1 + \frac{4}{7} \mathcal{T}^{1/2} + \frac{16}{49} \mathcal{T} + \frac{136}{15435} \mathcal{T}^{3/2} + \dots \quad \text{for } \mathcal{T} \ll 1. \quad (4.1)$$

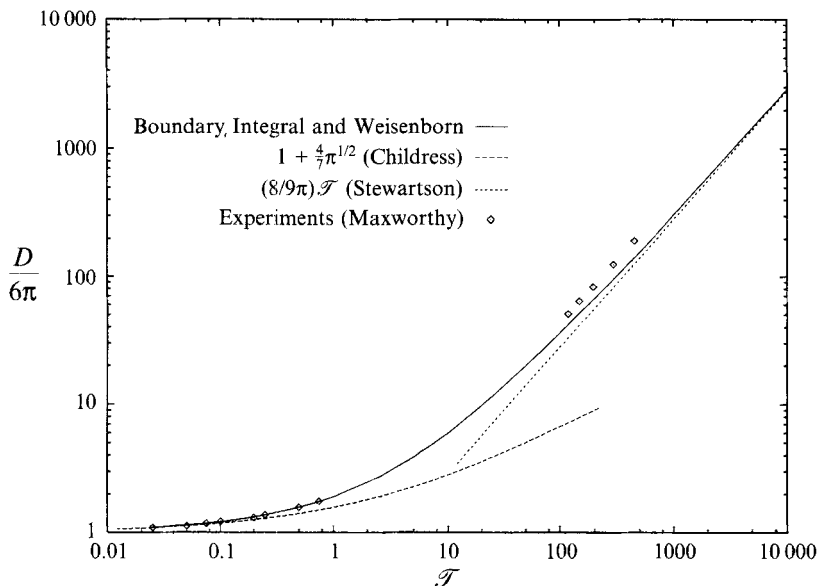


FIGURE 5. Drag on a rigid sphere versus Taylor number determined using: (i) the boundary integral method described here and a multipole expansion (Weisenborn 1985) (solid line); (ii) experimental results of Maxworthy (1965, 1970) (symbols); (iii) matched asymptotic expansion for $\mathcal{T} \ll 1$ (Childress 1964) (heavy dashed line); (iv) inviscid geostrophic analysis for $\mathcal{T} \gg 1$ (Stewartson 1952) (light dashed line).

For large Taylor numbers, Weisenborn does not provide an explicit formula for the drag, but rather presents tabulated data. The comparison between the drag determined using the boundary integral method and Weisenborn's results are within 0.5% over the Taylor number range shown in the figure. Both results are represented by the solid curve in figure 5.

A simple relationship for the drag as a function of Taylor number is given by the empirical formula

$$\frac{D}{6\pi} = 1 + \frac{4}{7} \mathcal{T}^{1/2} + \frac{8}{9\pi} \mathcal{T}, \quad (4.2)$$

which combines the low- and high-Taylor-number asymptotic limits. This formula is within 5% of the boundary integral and Weisenborn results for *all* Taylor numbers.

Maxworthy's experimental measurements (1965, 1970) are shown with symbols in figure 5. The results are in good agreement with the theoretical drag predictions for small Taylor number. Data for large Taylor number were obtained from the 1970 paper (p. 464 §3ii). In our notation, Maxworthy's empirical formula, representing data extrapolated to an unbounded system, is $D/6\pi = 0.433 \mathcal{T}$ for the parameter range $117 < \mathcal{T} < 445$ and $0.005 < \mathcal{R}_o < 0.1$. However, as discussed by previous researchers, the theoretical predictions are approximately 25% less than the measured drag values for the high-Taylor-number experiments. The reason for the discrepancy remains unanswered.

Figure 6 presents the components of the surface traction $\mathbf{n} \cdot \mathbf{T} = (F_\rho, F_\phi, F_\theta)$, expressed relative to a *spherical* coordinate system, for Taylor numbers $50 < \mathcal{T} < 5000$. Viscous stresses associated with the swirling motions induced by the rise of the particle generate an azimuthal stress F_ϕ on the particle surface; this stress vanishes in the Stokes flow limit. In the high-Taylor-number limit, thin Ekman boundary layers

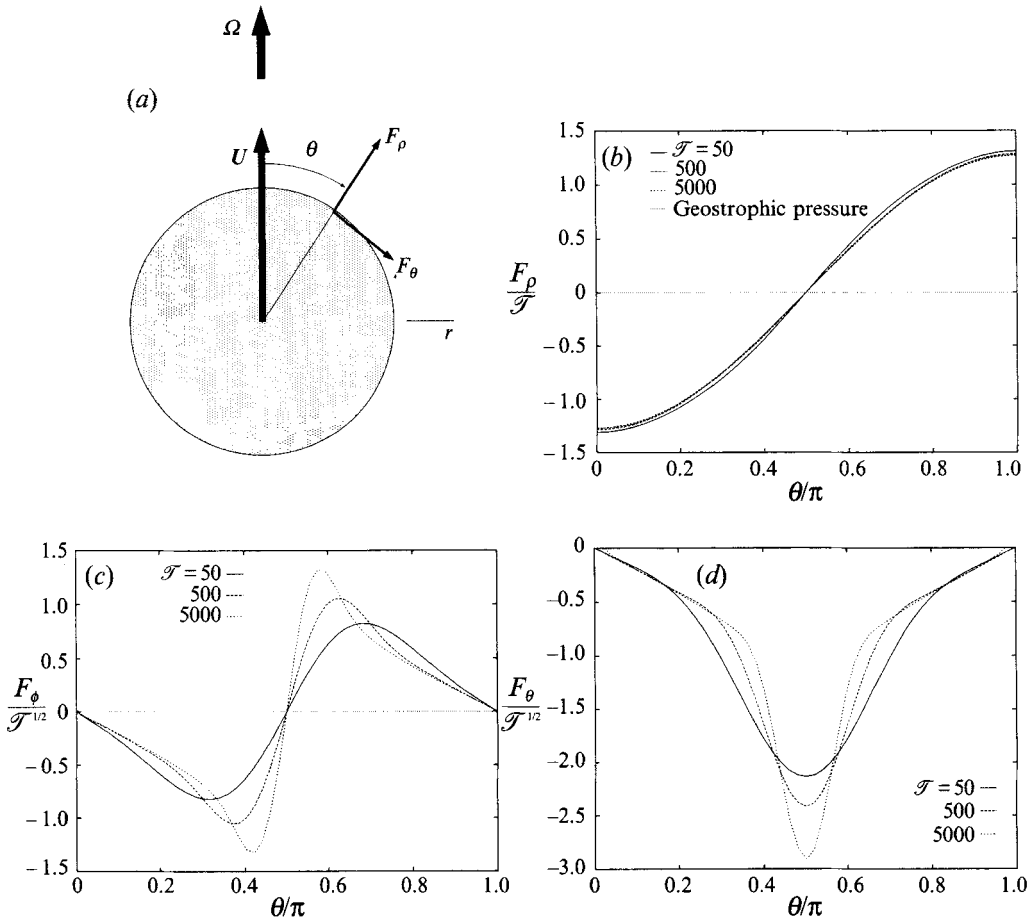


FIGURE 6. Surface traction, expressed in spherical coordinates (F_ρ, F_ϕ, F_θ), as a function of Taylor number ($\mathcal{T} = 50, 500, 5000$): (a) geometry, (b) F_ρ/\mathcal{T} , (c) $F_\phi/\mathcal{T}^{1/2}$, (d) $F_\theta/\mathcal{T}^{1/2}$. The geostrophic pressure (Stewartson 1952) on the surface of a sphere is $p = -(4\mathcal{T}/\pi) \cos \theta$ (using the scaling of this paper).

develop with a nominal thickness $\mathcal{T}^{-1/2}$. Consequently, the governing equations suggest that the pressure increases as \mathcal{T} and viscous stresses increase as $\mathcal{T}^{1/2}$. The pressure thus makes the largest contribution to the normal component of the stress, so that F_ρ should increase as \mathcal{T} . In fact, over the Taylor-number range shown in figure 6, the normal component of the traction is nearly identical with the geostrophic pressure distribution determined by Stewartson (1952). He found that for $\mathcal{T} \gg 1$, the pressure distribution at the surface of a sphere is $p = -(4\mathcal{T}/\pi) \cos \theta$, when expressed using the scalings of this paper. The azimuthal and meridional stress components are strictly viscous in character and scale as $\mathcal{T}^{1/2}$ in the high-Taylor-number limit. These scalings collapse the data as demonstrated in figure 6.

The flow field is illustrated as a function of increasing Taylor number in figures 7 and 8. Figure 7 shows streamlines plotted relative to a reference frame fixed to the particle and projected onto the (r, z) -plane. (The particle is fixed and a uniform flow approaches from large distances upstream. We have chosen this alternative frame of reference to illustrate the recirculating region.) Figure 8 presents contours of the

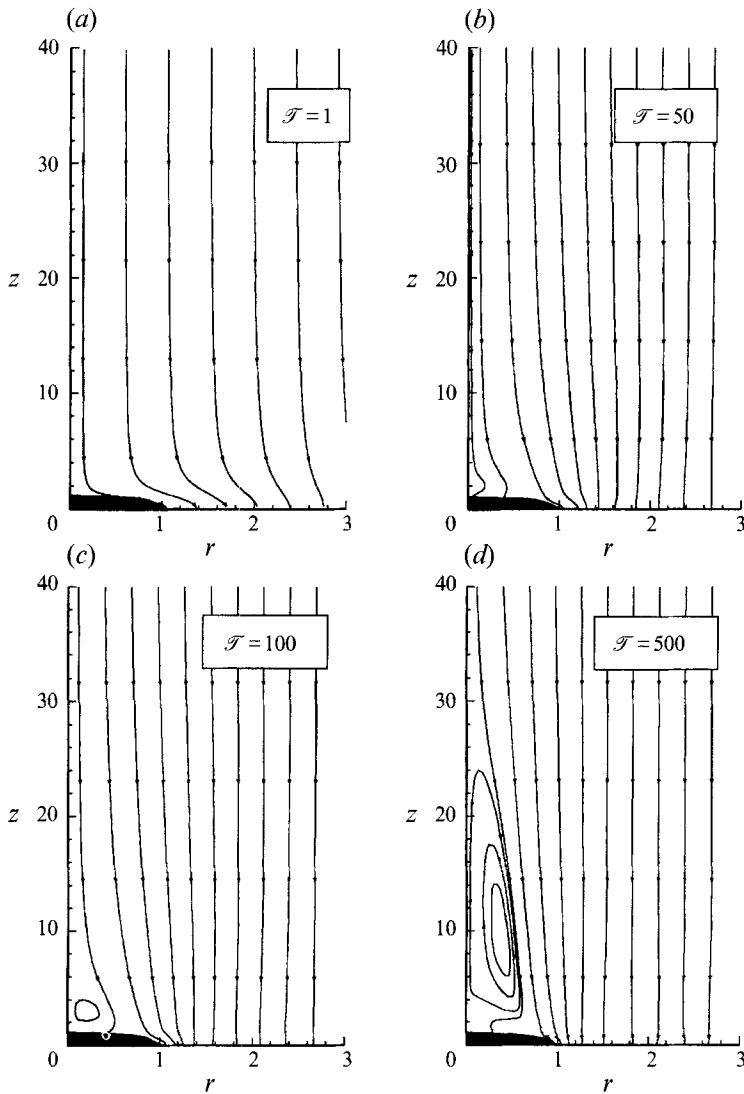


FIGURE 7. Streamlines shown relative to a reference frame attached to the particle and projected into the (r, z) -plane for (a) $\mathcal{T} = 1$, (b) $\mathcal{T} = 50$, (c) $\mathcal{T} = 100$, (d) $\mathcal{T} = 500$. Note that the axes are distorted and that a similar structure appears below the particle. For $\mathcal{T} > 50$, a recirculating region appears and increases in size with increasing Taylor number. For $\mathcal{T} < 50$, the flow appears qualitatively as a distorted Stokes flow. The swirling motion associated with this flow is shown in figure 8.

swirl angular velocity v/r ; where $v/r = \text{constant}$, the fluid is locally undergoing a solid-body rotation.

The streamline portraits illustrate that a critical Taylor number $\mathcal{T}_c \approx 50$ exists at which qualitative changes to the flow field occur. The flow field for small Taylor numbers $\mathcal{T} < \mathcal{T}_c$ is slightly distorted from that of a uniform Stokes flow ($\mathcal{T} = 0$) past a sphere with a superimposed swirling motion. The Coriolis force causes the swirl to change directions fore/aft of the particle.

For large Taylor numbers $\mathcal{T} > \mathcal{T}_c$, a columnar flow structure suggestive of a viscous Taylor column or Taylor slug is established. The flow field develops *detached*

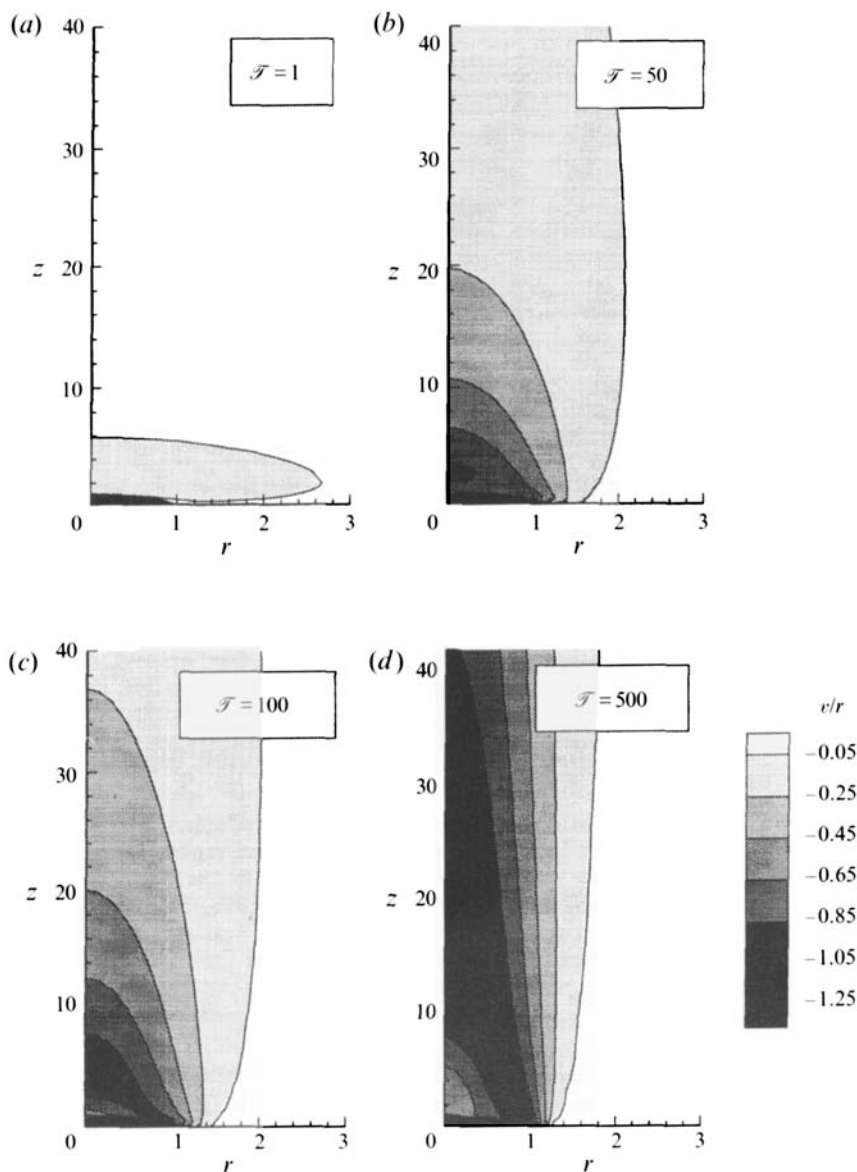


FIGURE 8. Contours of swirl angular velocity v/r measured relative to the solid-body rotation rate for (a) $\mathcal{T} = 1$, (b) $\mathcal{T} = 50$, (c) $\mathcal{T} = 100$, (d) $\mathcal{T} = 500$. A similar structure, but with oppositely directed swirl, appears below the particle. The recirculating regions and geostrophic regions are in nearly solid-body rotation moving with $O(1)$ angular velocities. The narrow region of steepening contours corresponds to the Stewartson layer.

recirculating regions fore and aft of the particle which grow in length and move farther from the particle as the Taylor number increases (figure 7c,d). The fluid remains confined within the recirculating regions and does not mix with the fluid whose streamlines approach from upstream. The magnitude of the recirculating velocities is approximately 10% of the imposed flow velocity. The recirculating region deflects fluid away from the centreline and redirects it along the sides of a cylinder which circumscribes the particle. The flow field between the recirculating

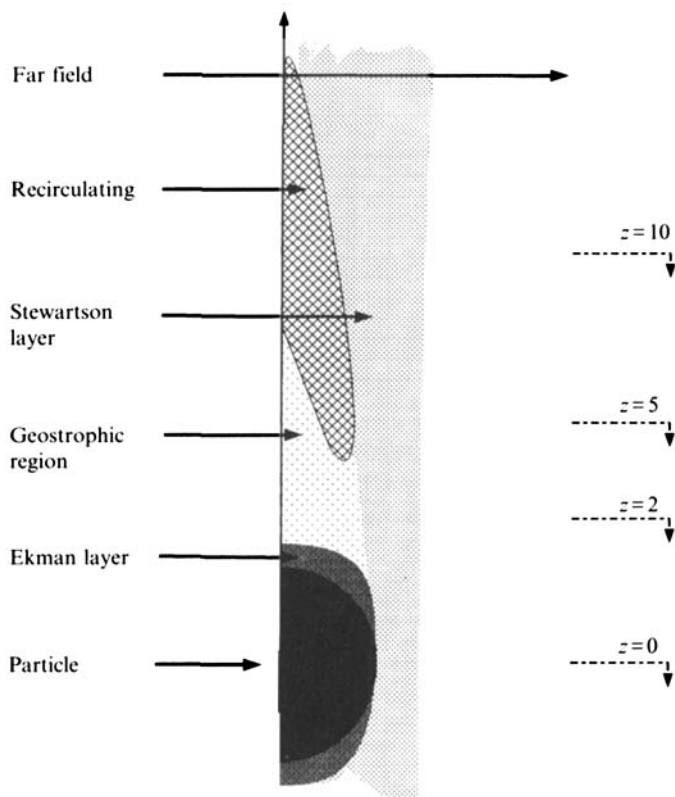


FIGURE 9. Regions in the flow field of a particle translating along the axis of a fluid in solid-body rotation when $\mathcal{T} > 50$: Ekman layer, geostrophic region, recirculating region, far field, Stewartson layer. (The horizontal and vertical scales are distorted.) Flow in the region we refer to as 'geostrophic' has attributes consistent with Moore & Saffman's (1969) analysis, which coupled geostrophic interior/exterior flows via viscous boundary layers. Also indicated are the approximate axial positions of radial slices corresponding to figure 10. Note that the Ekman layer thickens as the equator is approached, which is not indicated in the figure.

zone and the particle has a plug-like axial flow, nearly solid-body swirl velocity, and very weak radial velocity. These are features consistent with the interior geostrophic flow field described by Moore & Saffman (1969). The small flux of fluid entering this geostrophic region is drained by narrow Ekman layers adjacent to the particle surface. These flow features were also described by Vedensky & Ungarish (1994) for a rigid disc translating along the rotation axis.

For finite Taylor numbers ($\mathcal{T} \neq 0$), oppositely directed swirl velocities are generated fore and aft of the particle (figure 8). The region in front of (behind) the translating particle has swirl velocities, measured in the laboratory frame, less (greater) than the bulk rotation rate. As the Taylor number increases, the swirl velocity contours elongate in the direction of the rotation axis and concentrate within a narrow band along the edge of the Taylor column (figure 8*c,d*). This narrow layer corresponds to the Stewartson layer. The velocity contours suggest that much of the Taylor column is in nearly solid-body rotation relative to the bulk fluid, and that the swirling motion decays rapidly to the solid-body rotation rate within a narrow layer forming the column boundary.

The qualitative picture of the flow structure ($\mathcal{T} > 50$) is sketched in figure 9 which

identifies five distinct regions of the flow field and is modelled on the discussion given by Maxworthy (1970). Nearest the particle is a thin *Ekman* layer which matches the swirl velocity within the Taylor column to the particle velocity. This boundary layer transports fluid from within the Taylor column around the particle by means of Ekman pumping. The Taylor column consists of two domains which extend along the rotation axis. (i) A nearly *geostrophic* region where the fluid motion conforms approximately to the constraints of the Taylor–Proudman theorem – an $O(1)$ nearly uniform rotational motion, a weak plug-like axial flow, and a very weak radial flow. We refer to this region as geostrophic since our numerical results are in good agreement with Moore & Saffman's (1969) analysis based upon geostrophic interior/exterior regions coupled via Stewartson boundary layers. (ii) A *recirculating* flow region which bounds the Taylor column and deflects flow around the particle. Clearly the Taylor column is not 'stagnant', as it has been occasionally characterized in the literature. Finally, the *far field* is matched to the interior flow through a shear transition or *Stewartson* layer.

Figure 10 shows velocity components as a function of radial position at various axial positions indicated in figure 9 ($\mathcal{T} = 500$). The velocity profile at $z = 10$ passes through the recirculating region, at $z = 2$ passes through the geostrophic region, and at $z = 0$ passes through the particle ($r < 1$). The Stewartson layer, which appears in all velocity profiles as the region with large radial gradients, is centred near $r = 1$ and slowly broadens with increasing z .

In figure 10 we observe that the axial and swirl velocities are $O(1)$ throughout most of the Taylor column region; the radial velocities are much weaker with magnitude $O(10^{-2})$. Similar velocity magnitudes are observed over the entire range of Taylor numbers ($\mathcal{T} > \mathcal{T}_c$) and are consistent with the analytical estimates for the unbounded geometry developed by Moore & Saffman (1969, equation (8.14)). The qualitative features of these velocity fields are consistent with Maxworthy's (1970, figure 7) experimental results. (In a bounded geometry where the Taylor column spans the entire fluid depth, the swirl velocities increase as $\mathcal{T}^{1/2}$ in the high-Taylor-number limit owing to vortex stretching and compression that occurs near the lower and upper boundaries, respectively.)

Figure 10 demonstrates that fluid within the geostrophic region ($z = 2$) moves with the axial velocity of the particle and undergoes a nearly solid-body rotation with angular velocity $|v/r| \approx 0.6$ for $\mathcal{T} = 500$. The recirculating region ($z = 10$) also moves with a nearly solid-body rotation, but with an angular velocity $|v/r| \approx 1.0$. Within the Stewartson layer, the axial velocity exceeds the far-field velocity by a factor of more than two in the region adjacent to the particle. This increased velocity within a relatively narrow region sustains the volume flux generated as fluid is deflected around the core of the Taylor column. The radial extent of the Stewartson layer slowly broadens and the maximum axial velocity decreases with increasing z . All the velocity components exhibit large gradients along the radial direction.

The sizes of the different flow regions indicated in figure 9 depend on the magnitude of the Taylor number. Maxworthy's (1968) measurements showed that the Taylor column length, defined as the largest distance from the sphere at which the velocity on the axis is equal to the speed of the body, increases as $\mathcal{T}/17$. We can estimate the length of the Taylor column, as well as the boundaries of other flow regions, by examining the centreline velocity $w(r = 0, z)$. Figure 11(a) shows the centreline velocity $w(r = 0, z)$ as a function of axial distance measured from the particle surface and scaled by the Taylor number as $(z - 1)/\mathcal{T}$. This scaling clearly identifies the geostrophic and recirculating regions. Figure 11(b) plots the centreline velocity versus

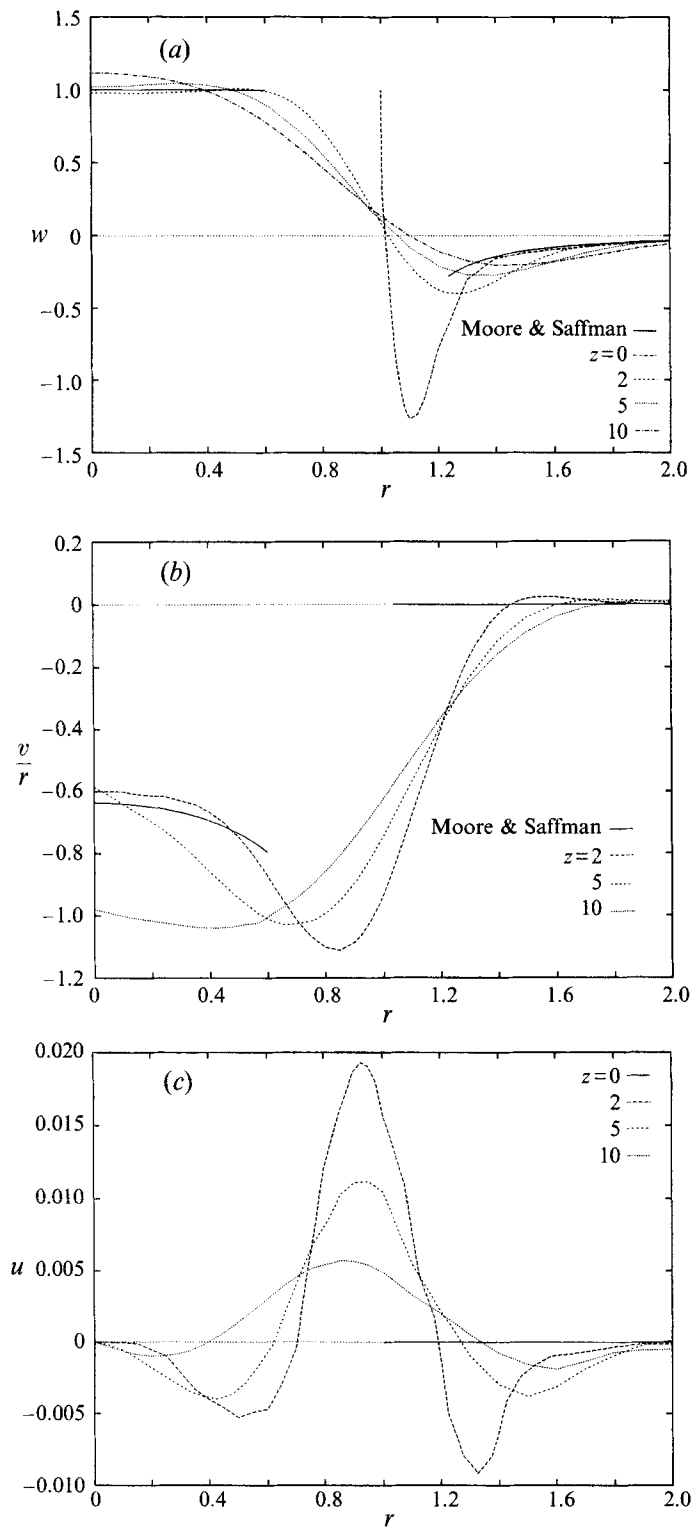


FIGURE 10. For caption see facing page.

axial distance scaled by the thickness of the Ekman layer $(z - 1)/\mathcal{T}^{-1/2}$. It is in this layer that the velocity in the geostrophic region is matched to the speed and rotation rate of the particle. The relative thicknesses of the Ekman layer, geostrophic and recirculating regions are shown in figure 12 as a function of Taylor number.

Using the centreline velocity, we may define the thickness of the Ekman layer adjacent to the particle as the distance where the axial velocity achieves its first minimum (see figure 11*b*). We find that the Ekman layer thins as $2.5\mathcal{T}^{-1/2}$ with increasing Taylor number. Adjacent to the Ekman layer is the geostrophic region in which the centreline velocity is nearly constant over a distance scaling as $0.006\mathcal{T}$. This region is a manifestation of the Taylor–Proudman constraint eliminating velocity variations in the axial direction. The magnitude of the axial velocity is only slightly less than the particle rise speed ($w = 0.98$ when $\mathcal{T} = 500$). This suggests that there is only a minimal flux into the region and that the Ekman suction which drains the region is weak. At a still larger axial distance is the recirculating region in which the centreline velocity exceeds the particle speed. The recirculating region forms the boundary of the Taylor column, which has a length measured from the particle surface increasing as $0.052\mathcal{T}$. This result agrees with the experiments of Maxworthy (1970) and the analysis of Vedensky & Ungarish. Beyond the recirculating zone is the far field in which the velocities viscously decay as $w(r = 0, z) \approx \mathcal{T}/z$.

4.2. Drag on a translating ellipsoid

We examine the effect of particle shape by studying the drag on a family of prolate ellipsoids. The surface is defined using $(r, z) = (\sin \theta, z_{max} \cos \theta)$ for $\theta = (0, \pi)$ so that lengths and the Taylor number are scaled by the equatorial radius. The aspect ratio (length/breadth) corresponds to the half-length of the particle along the rotation axis z_{max} .

Figure 13 illustrates the calculated drag as a function of Taylor number for aspect ratio $1 \leq z_{max} \leq 8$ and includes the drag on a thin disc determined in the analysis of Vedensky & Ungarish (1994). The drag is normalized to that of a unit sphere in a Stokes flow ($\mathcal{T} = 0$). The stability of the prolate shapes to small changes in orientation has not been studied.

In figure 13 we see that for a given shape the drag is a monotonically increasing function of Taylor number. At a fixed Taylor number, the increased drag with increasing aspect ratio is a consequence of the larger surface area of the particle. In the high-Taylor-number limit, the results for different aspect ratios all asymptote to the value $8\mathcal{T}/9\pi$. This result illustrates that the drag only depends on the cross-sectional area of the particle, a result noted by Moore & Saffman (1968). The flow

FIGURE 10. Velocity profiles of the (a) axial w , (b) angular swirl v/r , (c) radial u components plotted along radial slices at axial distances $z = 0, 2, 5, 10$ for $\mathcal{T} = 500$. The slice through $z = 0$ shows a large axial velocity in the Stewartson layer adjacent to the particle. (When $z = 0$, the particle extends to $r < 1$ and the velocities $u = v/r = 0$ based on symmetry.) The slice at $z = 2$ through the geostrophic region shows the velocity is plug-like with a nearly solid-body swirl ($r < 0.5$), while the section at $z = 10$ shows the recirculating region. Within Stewartson layers (centred at $r = 1$ and forming the sides of the Taylor column) the axial and radial velocities are a maximum and all the velocity components exhibit large gradients along the radial direction. Moore & Saffman's (1969, equation 8.14) high-Taylor-number prediction is shown by the solid curve. Their result is valid in regions outside the Stewartson layers and assumes that there is no Ekman pumping on the particle surface.

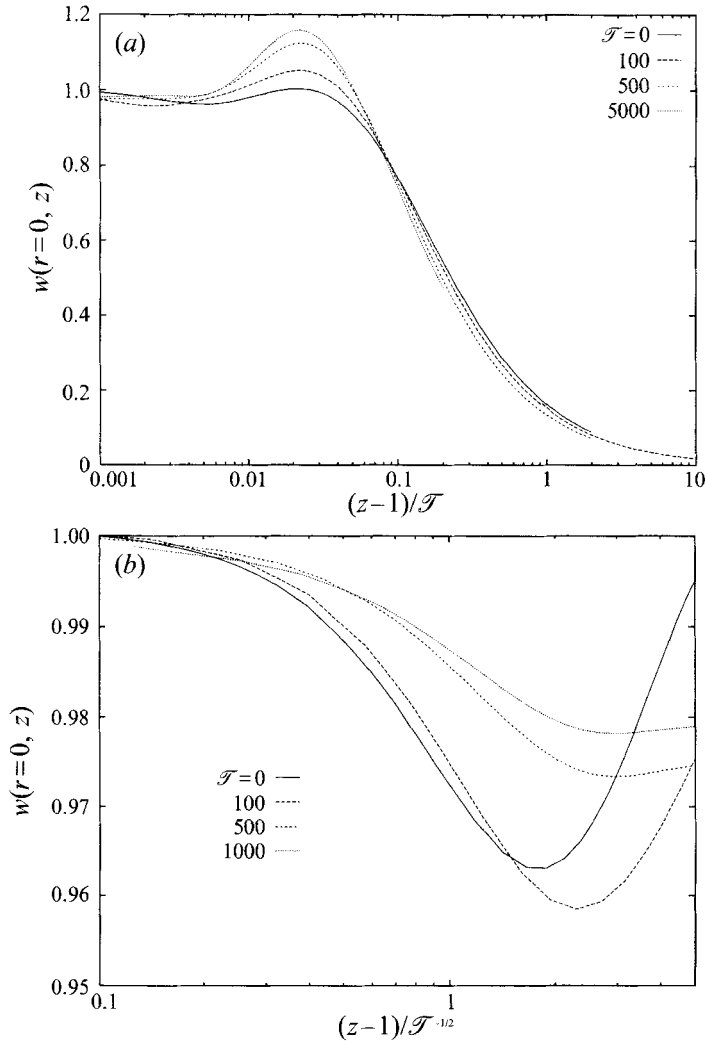


FIGURE 11. (a) Axial velocity $w(r=0, z)$ along the centreline measured from the particle surface $(z-1)$; (b) enlarged view near the particle surface showing the Ekman layer. (Note different scales in the two figures.) Figure (a) shows the geostrophic region in which the axial velocity is $w \approx 0.98$ the recirculating region where $w > 1$, and the far field where the axial velocity decays as $w \approx \mathcal{T}/z$. Figure (b) shows the Ekman layer which matches the flow in the geostrophic region to the particle speed.

fields for the translating ellipsoids have the qualitative features discussed in §4.1 and summarized in figure 9.

Finally, a simple formula for the drag as a function of Taylor number, suggested by Vedensky & Ungarish (1994) for low Taylor number, is obtained by combining the low- and high-Taylor-number asymptotic results to yield

$$\frac{D}{6\pi} = \frac{D_s}{6\pi} \left(1 + \frac{4 D_s}{7 6\pi} \mathcal{T}^{1/2} \right) + \frac{8}{9\pi} \mathcal{T}, \quad (4.3)$$

where D is the dimensionless drag and D_s is the dimensionless Stokes drag on the ellipsoidal shape. For aspect ratios less than 4, this simple formula is in excellent

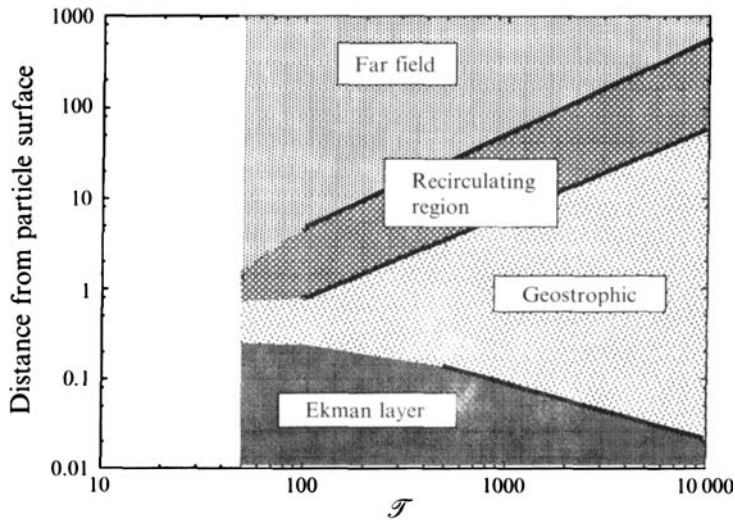


FIGURE 12. Distance from the particle surface ($z - 1$), measured along the centreline, of the boundaries between different regions of the flow. For sufficiently large Taylor number, the height of the Ekman layer scales as $2.5\mathcal{T}^{-1/2}$, the geostrophic region as $0.006\mathcal{T}$ and the recirculating region as $0.052\mathcal{T}$. Data points are based on the centreline velocity as described in the text.

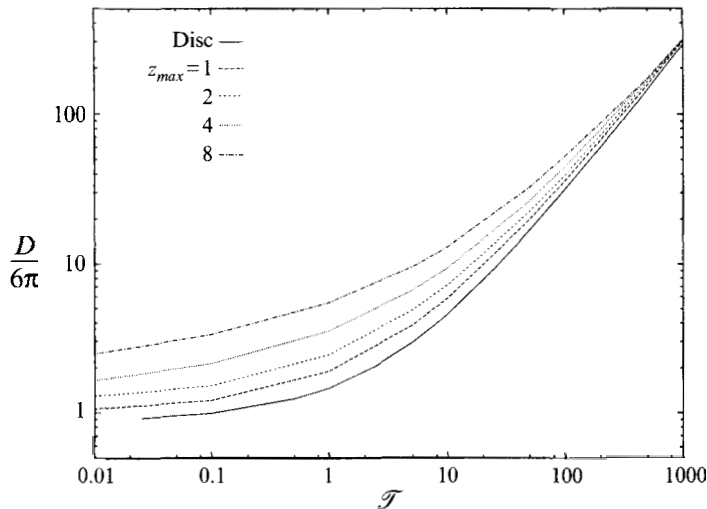


FIGURE 13. Drag on spheroidal particles and on a thin disc (from Vedensky & Ungarish 1994). The particle half-length (aspect ratio) is denoted z_{max} , and the lengths are scaled by the equatorial radius. For $\mathcal{T} \gg 1$ the drag does not depend on the particle shape.

agreement with the numerical results for all Taylor numbers. For larger aspect ratios, the approximation works well for both high and low Taylor numbers, but is less accurate for moderate values of the Taylor number.

We would like to thank Dr John W.M. Bush for many helpful conversations, in particular conversations which motivated this research, Professor Howard W. Emmons for his patience discussing the dynamics of rotating fluids, and Dr Oliver G. Harlen for assistance with the asymptotic approximations developed in Appendix C. Also,

H.A.S. gratefully acknowledges support from NSF-Presidential Young Investigator Award CTS-8957043.

Appendix A. Reciprocal theorem and related identities

We derive a reciprocal theorem for the linearized equations governing rotating viscous flow leading to an integral equation representation for the velocity field. Also we establish a reciprocal relation for the Green's function.

Consider two solenoidal vector fields defined within a volume V , bounded by surface S . Let $\{\mathbf{u}, \mathbf{T} \equiv -p\mathbf{I} + (\nabla\mathbf{u} + \nabla\mathbf{u}^t), \mathbf{f}\}$ satisfy the physical system of equations

$$2\mathcal{T}\boldsymbol{\Omega} \wedge \mathbf{u} = -\nabla p + \nabla^2\mathbf{u} + \mathbf{f} = \nabla \cdot \mathbf{T} + \mathbf{f} \quad \text{and} \quad \nabla \cdot \mathbf{u} = 0. \quad (\text{A } 1)$$

Similarly let $\{\hat{\mathbf{u}}, \hat{\mathbf{T}} \equiv -\hat{p}\mathbf{I} + (\nabla\hat{\mathbf{u}} + \nabla\hat{\mathbf{u}}^t), \hat{\mathbf{f}}\}$ satisfy the adjoint equations

$$-2\mathcal{T}\boldsymbol{\Omega} \wedge \hat{\mathbf{u}} = -\nabla\hat{p} + \nabla^2\hat{\mathbf{u}} + \hat{\mathbf{f}} = \nabla \cdot \hat{\mathbf{T}} + \hat{\mathbf{f}} \quad \text{and} \quad \nabla \cdot \hat{\mathbf{u}} = 0. \quad (\text{A } 2)$$

Subtracting the inner product of \mathbf{u} with (A 2) from the inner product of $\hat{\mathbf{u}}$ with (A 1), and using the vector identity $(\boldsymbol{\Omega} \wedge \mathbf{u}) \cdot \hat{\mathbf{u}} = -(\boldsymbol{\Omega} \wedge \hat{\mathbf{u}}) \cdot \mathbf{u}$ gives

$$0 = \nabla \cdot (\mathbf{T} \cdot \hat{\mathbf{u}}) - \nabla \cdot (\hat{\mathbf{T}} \cdot \mathbf{u}) + \mathbf{f} \cdot \hat{\mathbf{u}} - \hat{\mathbf{f}} \cdot \mathbf{u}, \quad (\text{A } 3)$$

where the sign change preceding \mathcal{T} in the adjoint equation eliminates the cross-product terms. Integrating (A 3) over the fluid volume V and applying the divergence theorem with normal \mathbf{n} directed *into* V yields the reciprocal identity

$$0 = \int_S \left[-\mathbf{n} \cdot \mathbf{T} \cdot \hat{\mathbf{u}} + \mathbf{n} \cdot \hat{\mathbf{T}} \cdot \mathbf{u} \right] dS + \int_V \left[\hat{\mathbf{u}} \cdot \mathbf{f} - \mathbf{u} \cdot \hat{\mathbf{f}} \right] dV, \quad (\text{A } 4)$$

which is analogous to the reciprocal theorem for Stokes equations.

General case: To develop an integral equation, identify $\hat{\mathbf{u}}$ with the flow due to a point force located at $\boldsymbol{\xi}$ by choosing $\hat{\mathbf{f}} = \hat{\mathbf{e}} \delta(\mathbf{x} - \boldsymbol{\xi})$ where $\hat{\mathbf{e}}$ is a constant vector. The fundamental solution of (A 2) is represented by

$$\hat{\mathbf{u}}(\mathbf{x}) = \mathbf{G}(\mathbf{x}|\boldsymbol{\xi}; \mathcal{T}) \cdot \hat{\mathbf{e}} \quad \text{and} \quad \hat{\mathbf{T}}(\mathbf{x}) = \mathbf{H}(\mathbf{x}|\boldsymbol{\xi}; \mathcal{T}) \cdot \hat{\mathbf{e}}. \quad (\text{A } 5)$$

Substituting equations (A 5) into (A 4) and eliminating the arbitrary forcing $\hat{\mathbf{e}}$ yields

$$\left. \begin{array}{l} \boldsymbol{\xi} \in V : \quad \mathbf{u}(\boldsymbol{\xi}) \\ \boldsymbol{\xi} \in S : \quad \frac{1}{2}\mathbf{u}(\boldsymbol{\xi}) \\ \boldsymbol{\xi} \notin V : \quad \mathbf{0} \end{array} \right\} = \int_V \mathbf{f} \cdot \mathbf{G}(\mathbf{x}|\boldsymbol{\xi}; \mathcal{T}) dV_x - \int_S \left[\mathbf{n} \cdot \mathbf{T} \cdot \mathbf{G}(\mathbf{x}|\boldsymbol{\xi}; \mathcal{T}) - \mathbf{u} \cdot \mathbf{H}(\mathbf{x}|\boldsymbol{\xi}; \mathcal{T}) \right] dS_x, \quad (\text{A } 6)$$

provided the surface has Lyapunov smoothness. Setting $\mathbf{f} = \mathbf{0}$ we obtain equation (2.5).

Axisymmetric case: We can use the axial symmetry at the outset to directly develop an axisymmetric integral equation representation. We choose a cylindrical coordinate system and assume that the velocity and stress fields do not depend on the azimuthal coordinate ϕ . Define the components of the surface traction vector $\mathbf{n} \cdot \mathbf{T}$ expressed with respect to the cylindrical base vectors (r, ϕ, z) as $\mathbf{F} = (F_r, F_\phi, F_z)$. The components (in cylindrical coordinates) are not dependent on azimuthal position. Denote the solutions $\hat{\mathbf{u}}, \hat{\mathbf{T}}$ to the adjoint equation for a ring of point forces through $\boldsymbol{\xi} = (\eta, \zeta)$ as

$$\hat{\mathbf{u}}(\mathbf{x}) = \mathbf{M}(\mathbf{x}|\boldsymbol{\xi}; \mathcal{T}) \cdot \hat{\mathbf{e}} \quad \text{and} \quad \hat{\mathbf{T}}(\mathbf{x}) = \mathbf{N}(\mathbf{x}|\boldsymbol{\xi}; \mathcal{T}) \cdot \hat{\mathbf{e}}, \quad (\text{A } 7)$$

where \hat{e} is a constant vector in cylindrical coordinates and $\hat{f} = \hat{e} \delta(r-\eta)\delta(z-\zeta)/(2\pi\eta)$ is the forcing in the adjoint equation (A 2). The terms \hat{u} and \hat{T} , hence $\mathbf{M}(\mathbf{x}|\xi; \mathcal{T}) \cdot \hat{e}$ and $\mathbf{N}(\mathbf{x}|\xi; \mathcal{T}) \cdot \hat{e}$, also do not depend on azimuthal angle ϕ .

If we take $\mathbf{f} = \mathbf{0}$ and the surface element in (A 4) to be $dS = 2\pi r ds$ with $ds^2 = dr^2 + dz^2$, the boundary integral expression, which incorporates axial symmetry, is

$$\left. \begin{array}{l} \xi \in V : \quad \mathbf{u}(\xi) \\ \xi \in S : \quad \frac{1}{2}\mathbf{u}(\xi) \\ \xi \notin V : \quad \mathbf{0} \end{array} \right\} = - \int_s 2\pi r [\mathbf{F} \cdot \mathbf{M}(\mathbf{x}|\xi; \mathcal{T}) - \mathbf{un} : \mathbf{N}(\mathbf{x}|\xi; \mathcal{T})] ds_x. \quad (\text{A } 8)$$

Reciprocity of the Green's function: Consider the point force responses to equation (A 1) and (A 2) with $\mathbf{f} = e\delta(\mathbf{x} - \xi)$ and $\hat{f} = \hat{e}\delta(\mathbf{x} - \hat{\xi})$. Equation (A 3) is written

$$\nabla \cdot (\mathbf{T} \cdot \hat{\mathbf{u}}) - \nabla \cdot (\hat{\mathbf{T}} \cdot \mathbf{u}) + e \cdot \hat{\mathbf{u}} \delta(\mathbf{x} - \xi) - \hat{e} \cdot \mathbf{u} \delta(\mathbf{x} - \hat{\xi}) = 0. \quad (\text{A } 9)$$

The fundamental solution of (A 2) is $\hat{\mathbf{u}}(\mathbf{x}) = \mathbf{G}(\mathbf{x}|\hat{\xi}; \mathcal{T}) \cdot \hat{e}$. By comparing equations (A 1) and (A 2), we may write $\mathbf{u}(\mathbf{x}) = \mathbf{G}(\mathbf{x}|\xi; -\mathcal{T}) \cdot e$. Integrating (A 9) over the fluid volume and using the divergence theorem yields

$$e \cdot \mathbf{G}(\xi|\hat{\xi}, \mathcal{T}) \cdot \hat{e} = \hat{e} \cdot \mathbf{G}(\hat{\xi}|\xi; -\mathcal{T}) \cdot e. \quad (\text{A } 10)$$

Therefore, we may conclude that

$$\mathbf{G}'(\xi|\hat{\xi}; \mathcal{T}) = \mathbf{G}(\hat{\xi}|\xi; -\mathcal{T}), \quad (\text{A } 11)$$

which establishes a reciprocity relation for this Green's function.

Appendix B. Disturbance Green's function

The diagonal terms of the Green's function \mathbf{M} have a logarithmic singularity as $(r, z) \rightarrow (\eta, \zeta)$, creating numerical problems when the integrals defining the Green's function are evaluated near the singular point. By subtracting the singular Stokeslet ($\mathcal{T} = 0$) contribution, the integral expression which remains, $\mathbf{M}^d \equiv \mathbf{M} - \mathbf{M}^{\text{Stokes}}$, is then convergent everywhere.

In this appendix we first show how to recover the common form of the axisymmetric Stokeslet (e.g. Pozrikidis 1992) containing elliptic integrals. We then form the non-singular disturbance Green's function \mathbf{M}^d by removing the singular Stokeslet.

B.1. Axisymmetric Stokeslet

The known axisymmetric Stokeslet solution follows from equation (3.24) in two steps. First contour integration of the axial wavenumber n yields

$$\mathbf{M}_{rr}^{\text{Stokes}} = \frac{1}{8\pi} \int_0^\infty (1 - k|z - \zeta|) e^{-k|z-\zeta|} J_1(rk) J_1(\eta k) dk, \quad (\text{B } 1a)$$

$$\mathbf{M}_{rz}^{\text{Stokes}} = \frac{1}{8\pi} \int_0^\infty (z - \zeta) k e^{-k|z-\zeta|} J_1(rk) J_0(\eta k) dk, \quad (\text{B } 1b)$$

$$\mathbf{M}_{\phi\phi}^{\text{Stokes}} = \frac{1}{4\pi} \int_0^\infty e^{-k|z-\zeta|} J_1(rk) J_1(\eta k) dk, \quad (\text{B } 1c)$$

$$\mathbf{M}_{zr}^{\text{Stokes}} = -\frac{1}{8\pi} \int_0^\infty (z - \zeta) k e^{-k|z-\zeta|} J_0(rk) J_1(\eta k) dk, \quad (\text{B } 1d)$$

$$M_{zz}^{Stokes} = \frac{1}{8\pi} \int_0^\infty (1 + k|z - \zeta|) e^{-k|z - \zeta|} J_0(rk) J_0(\eta k) dk. \quad (\text{B } 1e)$$

These expressions can be simplified using known identities (Gradshteyn 1965, eq. 6.612-3; Abramowitz & Stegun 1970, eq. 8.13; Eason, Noble & Sneddon 1955 note the factor of $\pi/2$ in the definition of the elliptic integrals) to arrive at the familiar form involving elliptic integrals:

$$M_{rr}^{Stokes} = \frac{1}{8\pi^2 r \eta B} \times \left[(r^2 + \eta^2 + 2(z - \zeta)^2) K(k) - \frac{(r^2 - \eta^2)^2 + 3(r^2 + \eta^2)(z - \zeta)^2 + 2(z - \zeta)^4}{A^2} E(k) \right], \quad (\text{B } 2a)$$

$$M_{rz}^{Stokes} = \frac{z - \zeta}{8\pi^2 r B} \left[K(k) - \frac{\eta^2 - r^2 + (z - \zeta)^2}{A^2} E(k) \right], \quad (\text{B } 2b)$$

$$M_{\phi\phi}^{Stokes} = \frac{B}{4\pi^2 r \eta} \left[\frac{r^2 + \eta^2 + (z - \zeta)^2}{B^2} K(k) - E(k) \right], \quad (\text{B } 2c)$$

$$M_{zr}^{Stokes} = -\frac{z - \zeta}{8\pi^2 \eta B} \left[K(k) + \frac{\eta^2 - r^2 - (z - \zeta)^2}{A^2} E(k) \right], \quad (\text{B } 2d)$$

$$M_{zz}^{Stokes} = \frac{1}{4\pi^2 B} \left[K(k) + \frac{(z - \zeta)^2}{A^2} E(k) \right], \quad (\text{B } 2e)$$

where $K(k)$ and $E(k)$ are elliptic integrals of the first and second kind, respectively, and

$$A^2 = (r - \eta)^2 + (z - \zeta)^2, \quad B^2 = (r + \eta)^2 + (z - \zeta)^2, \quad k^2 = 4r\eta/B^2.$$

The reciprocity relation (i.e. interchanging source and receiver) is simply the transpose of the matrix \mathbf{M}^{Stokes} . Terms on the diagonal, M_{rr}^{Stokes} , $M_{\phi\phi}^{Stokes}$ and M_{zz}^{Stokes} , have a logarithmic singularity for $(r, z) \rightarrow (\eta, \zeta)$, while the off-diagonal terms are not singular.

B.2. Disturbance Green's function

The disturbance Green's function is specified by subtracting the Stokeslet $\mathbf{M}^d = \mathbf{M} - \mathbf{M}^{Stokes}$ to produce

$$M_{rr}^d = \frac{1}{2\pi} \int_0^\infty k \left[-\frac{c(k^2 - c^2)}{A_1} e^{-c|z - \zeta|} + 2\text{Re} \left\{ \frac{iN(k^2 + N^2)}{A_2} e^{iN|z - \zeta|} \right\} - \frac{1 - k|z - \zeta|}{4} e^{-k|z - \zeta|} \right] J_1(kr) J_1(k\eta) dk, \quad (\text{B } 3a)$$

$$M_{r\phi}^d = \frac{1}{2\pi} \int_0^\infty -2\mathcal{T} k \left[-\frac{c}{A_1} e^{-c|z - \zeta|} + 2\text{Re} \left\{ \frac{iN}{A_2} e^{iN|z - \zeta|} \right\} \right] J_1(kr) J_1(k\eta) dk, \quad (\text{B } 3b)$$

$$M_{rz}^d = \frac{1}{2\pi} \int_0^\infty \text{sgn}(z - \zeta) k^2 \left[\frac{k^2 - c^2}{A_1} e^{-c|z - \zeta|} + 2\text{Re} \left\{ \frac{k^2 + N^2}{A_2} e^{iN|z - \zeta|} \right\} - \frac{k|z - \zeta|}{4} e^{-k|z - \zeta|} \right] J_1(kr) J_0(k\eta) dk, \quad (\text{B } 3c)$$

$$M_{\phi r}^d = \frac{1}{2\pi} \int_0^\infty 2\mathcal{F}k \left[-\frac{c}{A_1} e^{-c|z-\zeta|} + 2\text{Re} \left\{ \frac{iN}{A_2} e^{iN|z-\zeta|} \right\} \right] J_1(kr)J_1(k\eta) dk, \quad (\text{B } 3d)$$

$$M_{\phi\phi}^d = \frac{1}{2\pi} \int_0^\infty k \left[\frac{(k^2 - c^2)^2}{cA_1} e^{-c|z-\zeta|} + 2\text{Re} \left\{ \frac{i(k^2 + N^2)^2}{NA_2} e^{iN|z-\zeta|} \right\} - \frac{1}{2} e^{-k|z-\zeta|} \right] J_1(kr)J_1(k\eta) dk, \quad (\text{B } 3e)$$

$$M_{\phi z}^d = \frac{1}{2\pi} \int_0^\infty \text{sgn}(z - \zeta) 2\mathcal{F}k^2 \left[\frac{1}{A_1} e^{-c|z-\zeta|} + 2\text{Re} \left\{ \frac{1}{A_2} e^{iN|z-\zeta|} \right\} \right] J_1(kr)J_0(k\eta) dk, \quad (\text{B } 3f)$$

$$M_{zr}^d = \frac{1}{2\pi} \int_0^\infty -\text{sgn}(z - \zeta) k^2 \left[\frac{k^2 - c^2}{A_1} e^{-c|z-\zeta|} + 2\text{Re} \left\{ \frac{k^2 + N^2}{A_2} e^{iN|z-\zeta|} \right\} - \frac{k|z - \zeta|}{4} e^{-k|z-\zeta|} \right] J_0(kr)J_1(k\eta) dk, \quad (\text{B } 3g)$$

$$M_{z\phi}^d = \frac{1}{2\pi} \int_0^\infty \text{sgn}(z - \zeta) 2\mathcal{F}k^2 \left[\frac{1}{A_1} e^{-c|z-\zeta|} + 2\text{Re} \left\{ \frac{1}{A_2} e^{iN|z-\zeta|} \right\} \right] J_0(kr)J_1(k\eta) dk, \quad (\text{B } 3h)$$

$$M_{zz}^d = \frac{1}{2\pi} \int_0^\infty k^3 \left[\frac{k^2 - c^2}{cA_1} e^{-c|z-\zeta|} + 2\text{Re} \left\{ \frac{i(k^2 + N^2)}{NA_2} e^{iN|z-\zeta|} \right\} - \frac{1 + k|z - \zeta|}{4} e^{-k|z-\zeta|} \right] J_0(kr)J_0(k\eta) dk, \quad (\text{B } 3i)$$

where the functions A_1, A_2, c, N are defined in §3.2.

Appendix C. Asymptotic expression for M

In this appendix we derive the far-field asymptotic form of the Green's function valid for $\mathcal{F}^{-1/2}|z - \zeta| \gg 1$. It is first necessary to rescale the Green's function given in (3.22) by using the identity $\mathbf{M}(r, z|\eta, \zeta; \mathcal{F}) = \mathcal{F}^{1/2} \mathbf{M}(\mathcal{F}^{1/2}r, \mathcal{F}^{1/2}z|\mathcal{F}^{1/2}\eta, \mathcal{F}^{1/2}\zeta; \mathcal{F} = 1)$ to remove the explicit Taylor number dependence from the denominator. Then the Taylor number only appears as a multiplicative factor involving the positions r, η or $|z - \zeta|$. If we define $\chi \equiv \mathcal{F}^{1/2}|z - \zeta|/2 \gg 1$, the rescaled Green's function is

$$M_{rr} = \frac{\mathcal{F}^{1/2}}{2\pi} \int_0^\infty k \left[-\frac{c(k^2 - c^2)}{A_1} e^{-c2\chi} + 2\text{Re} \left\{ \frac{iN(k^2 + N^2)}{A_2} e^{iN2\chi} \right\} \right] \times J_1(k\mathcal{F}^{1/2}r)J_1(k\mathcal{F}^{1/2}\eta) dk, \quad (\text{C } 1a)$$

$$M_{r\phi} = \frac{\mathcal{F}^{1/2}}{2\pi} \int_0^\infty -2k \left[-\frac{c}{A_1} e^{-c2\chi} + 2\text{Re} \left\{ \frac{iN}{A_2} e^{iN2\chi} \right\} \right] J_1(k\mathcal{F}^{1/2}r)J_1(k\mathcal{F}^{1/2}\eta) dk, \quad (\text{C } 1b)$$

$$M_{rz} = \frac{\mathcal{F}^{1/2}}{2\pi} \int_0^\infty \text{sgn}(z - \zeta) k^2 \left[\frac{k^2 - c^2}{A_1} e^{-c2\chi} + 2\text{Re} \left\{ \frac{k^2 + N^2}{A_2} e^{iN2\chi} \right\} \right] \times J_1(k\mathcal{F}^{1/2}r)J_0(k\mathcal{F}^{1/2}\eta) dk, \quad (\text{C } 1c)$$

$$M_{\phi r} = \frac{\mathcal{F}^{1/2}}{2\pi} \int_0^\infty 2k \left[-\frac{c}{A_1} e^{-c2\chi} + 2\text{Re} \left\{ \frac{iN}{A_2} e^{iN2\chi} \right\} \right] J_1(k\mathcal{F}^{1/2}r)J_1(k\mathcal{F}^{1/2}\eta) dk, \quad (\text{C } 1d)$$

$$M_{\phi\phi} = \frac{\mathcal{T}^{1/2}}{2\pi} \int_0^\infty k \left[\frac{(k^2 - c^2)^2}{cA_1} e^{-c2\chi} + 2\text{Re} \left\{ \frac{i(k^2 + N^2)^2}{NA_2} e^{iN2\chi} \right\} \right] \\ \times J_1(k\mathcal{T}^{1/2}r)J_1(k\mathcal{T}^{1/2}\eta) dk, \quad (\text{C } 1\text{e})$$

$$M_{\phi z} = \frac{\mathcal{T}^{1/2}}{2\pi} \int_0^\infty \text{sgn}(z - \zeta)2k^2 \left[\frac{1}{A_1} e^{-c2\chi} + 2\text{Re} \left\{ \frac{1}{A_2} e^{iN2\chi} \right\} \right] \\ \times J_1(k\mathcal{T}^{1/2}r)J_0(k\mathcal{T}^{1/2}\eta) dk, \quad (\text{C } 1\text{f})$$

$$M_{zr} = \frac{\mathcal{T}^{1/2}}{2\pi} \int_0^\infty -\text{sgn}(z - \zeta)k^2 \left[\frac{k^2 - c^2}{A_1} e^{-c2\chi} + 2\text{Re} \left\{ \frac{k^2 + N^2}{A_2} e^{iN2\chi} \right\} \right] \\ \times J_0(k\mathcal{T}^{1/2}r)J_1(k\mathcal{T}^{1/2}\eta) dk, \quad (\text{C } 1\text{g})$$

$$M_{z\phi} = \frac{\mathcal{T}^{1/2}}{2\pi} \int_0^\infty \text{sgn}(z - \zeta)2k^2 \left[\frac{1}{A_1} e^{-c2\chi} + 2\text{Re} \left\{ \frac{1}{A_2} e^{iN2\chi} \right\} \right] \\ \times J_0(k\mathcal{T}^{1/2}r)J_1(k\mathcal{T}^{1/2}\eta) dk, \quad (\text{C } 1\text{h})$$

$$M_{zz} = \frac{\mathcal{T}^{1/2}}{2\pi} \int_0^\infty k^3 \left[\frac{k^2 - c^2}{cA_1} e^{-c2\chi} + 2\text{Re} \left\{ \frac{i(k^2 + N^2)}{NA_2} e^{iN2\chi} \right\} \right] \\ \times J_0(k\mathcal{T}^{1/2}r)J_0(k\mathcal{T}^{1/2}\eta) dk, \quad (\text{C } 1\text{i})$$

where c, N, A_1, A_2 are the roots given in equations (3.19), (3.20) and (3.23) with $\mathcal{T} = 1$.

In the limit $\chi \gg 1$, the two terms in the integrand of the Green's function can be estimated using Laplace's method. The major contribution to the integral comes from a small region around $k = 0$, with the remainder contributing exponentially small terms. The Taylor series expansion of the integrand in the neighbourhood of $k = 0$ makes use of $c \approx k^3/2 - 3/16 k^7$ and $N \approx (1 + i) + 3/8(-1 + i) k^2$. We define

$$\alpha = \left(\frac{2\mathcal{T}}{|z - \zeta|} \right)^{1/3} r \quad \text{and} \quad \beta = \left(\frac{2\mathcal{T}}{|z - \zeta|} \right)^{1/3} \eta.$$

The far-field estimate ($\chi \gg 1$) is straightforward provided $\alpha, \beta \ll 1$, corresponding to a position within a conical region near the z -axis, in which case we obtain

$$M_{rr} \sim -\frac{\sqrt[3]{2}}{8\pi} \mathcal{T}^{-2/3} |z - \zeta|^{-7/3} \int_0^\infty s^6 e^{-s^3} J_1(\alpha s) J_1(\beta s) ds, \quad (\text{C } 2\text{a})$$

$$M_{r\phi} \sim \frac{\sqrt[3]{4}}{8\pi} \mathcal{T}^{-1/3} |z - \zeta|^{-5/3} \int_0^\infty s^4 e^{-s^3} J_1(\alpha s) J_1(\beta s) ds, \quad (\text{C } 2\text{b})$$

$$M_{rz} \sim \frac{\text{sgn}(z - \zeta)\sqrt[3]{4}}{8\pi} \mathcal{T}^{-1/3} |z - \zeta|^{-5/3} \int_0^\infty s^4 e^{-s^3} J_1(\alpha s) J_0(\beta s) ds, \quad (\text{C } 2\text{c})$$

$$M_{\phi r} \sim -\frac{\sqrt[3]{4}}{8\pi} \mathcal{T}^{-1/3} |z - \zeta|^{-5/3} \int_0^\infty s^4 e^{-s^3} J_1(\alpha s) J_1(\beta s) ds, \quad (\text{C } 2\text{d})$$

$$M_{\phi\phi} \sim \frac{1}{4\pi} |z - \zeta|^{-1} \int_0^\infty s^2 e^{-s^3} J_1(\alpha s) J_1(\beta s) ds, \quad (\text{C } 2\text{e})$$

$$M_{\phi z} \sim \frac{1}{4\pi} (z - \zeta)^{-1} \int_0^\infty s^2 e^{-s^3} J_1(\alpha s) J_0(\beta s) ds, \quad (\text{C } 2\text{f})$$

$$M_{zr} \sim -\frac{\text{sgn}(z - \zeta)\sqrt[3]{4}}{8\pi} \mathcal{T}^{-1/3} |z - \zeta|^{-5/3} \int_0^\infty s^4 e^{-s^3} J_0(\alpha s) J_1(\beta s) ds, \quad (\text{C } 2\text{g})$$

$$M_{z\phi} \sim \frac{1}{4\pi} (z - \zeta)^{-1} \int_0^\infty s^2 e^{-s^3} J_0(\alpha s) J_1(\beta s) ds, \quad (\text{C } 2h)$$

$$M_{zz} \sim \frac{1}{4\pi} |z - \zeta|^{-1} \int_0^\infty s^2 e^{-s^3} J_0(\alpha s) J_0(\beta s) ds. \quad (\text{C } 2i)$$

The far-field response of a point force located on the origin corresponds to setting $(r, z) = 0$, hence $\alpha = 0$. In the limit $\beta \ll 1$ and $\chi \gg 1$, the velocity fields become

$$M_{zr} \sim \frac{\text{sgn}(\zeta)}{2\pi} \frac{\eta}{\zeta^2}, \quad M_{z\phi} \sim -\frac{\text{sgn}(\zeta)}{12\pi} \Gamma\left(\frac{1}{3}\right) \frac{(2\mathcal{F})^{1/3} \eta}{|\zeta|^{4/3}}, \quad M_{zz} \sim \frac{1}{4\pi} \frac{1}{|\zeta|},$$

which are valid in the far-field of a conical region around the z -axis.

REFERENCES

- ABRAMOWITZ, M. & STEGUN, I. A. 1970 *Handbook of Mathematical Functions*. Dover.
- BACHELOR, G. K. 1967 *An Introduction to Fluid Dynamics*. Cambridge University Press.
- BUSH, J. W., STONE, H. A. & BLOXHAM, J. B. 1993 Axial drop motion in rotating fluids. submitted.
- CHILDRESS, S. 1964 The slow motion of a sphere in a rotating, viscous fluid. *J. Fluid Mech.* **20**, 305–314.
- DENNIS, S. C. R., INGHAM, D. B. & SINGH, S. N. 1982 The slow translation of a sphere in a rotating viscous fluid. *J. Fluid Mech.* **117**, 251–267.
- EASON, G., NOBLE, B. & SNEDDON, I. 1955 On certain integrals of Lipschitz-Hankel type involving products of Bessel functions. *Phil. Trans. R. Soc. Lond. A* **247**, 529–551.
- GRADSHTEYN, I. S. & RYZHIK, I. M. 1965 *Table of Integrals, Series and Products*. Academic.
- GREENSPAN, H. P. 1968 *The Theory of Rotating Fluids*. Cambridge University Press.
- HERRON, I. H., DAVIS, S. H. & BRETHERTON, F. P. 1975 On the sedimentation of a sphere in a centrifuge. *J. Fluid Mech.* **68**, 209–234.
- HOCKING, L. M., MOORE, D. W. & WALTON, I. C. 1979 The drag on a sphere moving axially in a long rotating container. *J. Fluid Mech.* **90**, 781–793.
- HSU, H. W. 1981 *Separations By Centrifugal Phenomena*. John Wiley.
- KIM, S. & KARRILA, S. J. 1991 *Microhydrodynamics: Principles and Selected Applications*. Butterworth-Heinemann.
- LUCAS, S. K. 1994 Evaluating infinite integrals involving products of Bessel functions of arbitrary order. *J. Comput. Appl. Math.* (submitted).
- MAXWORTHY, T. 1965 An experimental determination of the slow motion of a sphere in a rotating, viscous fluid. *J. Fluid Mech.* **23**, 373–384.
- MAXWORTHY, T. 1968 The observed motion of a sphere through a short, rotating cylinder of fluid. *J. Fluid Mech.* **31**, 643–655.
- MAXWORTHY, T. 1970 The flow created by a sphere moving along the axis of a rotating, slightly-viscous fluid. *J. Fluid Mech.* **40**, 453–479.
- MOORE, D. W. & SAFFMAN, P. G. 1968 The rise of a body through a rotating fluid in a container of finite length. *J. Fluid Mech.* **31**, 635–642.
- MOORE, D. W. & SAFFMAN, P. G. 1969 The structure of vertical free shear layers in a rotating fluid and the motion produced by a slowly rising body. *Phil. Trans. R. Soc. Lond. A* **264**, 597–634.
- MORRISON, J. W. & MORGAN, G. W. 1956 The slow motion of a disc along the axis of a viscous, rotating liquid. Rep. 56207/8. Div. of Appl. Math. Brown University.
- MORSE, P. M. & FESHBACH, H. 1953 *Methods of Theoretical Physics*. McGraw-Hill.
- POZRIKIDIS, C. 1992 *Boundary Integral and Singularity Methods for Linearized Viscous Flow*. Cambridge University Press.
- PRITCHARD, W. G. 1969 The motion generated by a body moving along the axis of a uniformly rotating fluid. *J. Fluid Mech.* **39**, 443–464.
- SNEDDON, I. N. 1972 *The Use of Integral Transforms*. McGraw-Hill.
- STEWARTSON, K. 1952 On the slow motion of a sphere along the axis of a rotating fluid. *Proc. Camb. Phil. Soc.* **48**, 168–177.

- TAYLOR, G. I. 1922 The motion of a sphere in a rotating liquid. *Proc. R. Soc. Lond. A* **102**, 180–189.
- TAYLOR, G. I. 1923 Experiments on the motion of solid bodies in rotating fluids. *Proc. R. Soc. Lond. A* **104**, 213–219.
- UNGARISH, M. 1993 *Hydrodynamics of Suspensions*. Springer.
- VEDENSKY, D. & UNGARISH, M. 1994 The motion generated by a slowly rising disk in an unbounded rotating fluid for arbitrary Taylor number. *J. Fluid Mech.* **262**, 1–26.
- WEISENBORN, A. J. 1985 The drag on a sphere moving slowly in a rotating viscous fluid. *J. Fluid Mech.* **153**, 215–227.
- YOUNGREN, G. A. & ACRIVOS, A. 1975 Stokes flow past a particle of arbitrary shape: a numerical method of solution. *J. Fluid Mech.* **69**, 377–403.